ALMA MATER STUDIORUM
UNIVERSITÀ DI BOLOGNA

European Organization for Nuclear Research
Alma Mater Studiorum - Università di Bologna

Corso di Laurea in Ingegneria Energetica

Master Thesis

Analysis of the Stability Margin of the High Luminosity LHC Superconducting Cables with a Multi-Strand Model

Author:
Enrico Felcini

Supervisors:
Marco Breschi
Luca Bottura

2016

CERN-THESIS-2016-081
17/03/2016

Sommario

Al CERN (Centro Europeo per la Ricerca Nucleare), tra il 1998 e il 2008, è stato costruito il più grande e più potente collimatore di particelle del mondo. LHC (Large Hadron Collider) è la più grande infrastruttura scientifica mai realizzata per esplorare le nuove frontiere della fisica ad alta energia e coinvolge una comunità di 7000 scienziati da oltre 60 paesi. Le particelle accelerate vengono fatte collidere tra loro ad una velocità prossima a quella della luce. Questo processo permette di comprende le interazioni tra le diverse particelle e fornisce degli straordinari indizi sulle legge fondamentali della natura. Dopo le ultime incredibili scoperte, riguardanti il bosone di Higgs ed i penta-quarks, un ulteriore avanzamento tecnologico è necessario. Al fine di incrementare il proprio potenziale di ricerca, l' LCH avrà bisogno di un forte aggiornamento, intorno al 2020, per aumentare la propria luminosità (rateo di collisioni) di un fattore 10 rispetto al valore di progettazione originale (da 300 a 3000 fb^{-1}).Per una macchina così complessa ed ottimizzata come l' LHC, un aggiornamento di questo tipo richiede un accurato studio ed oltre 10 anni di implementazione. L'obiettivo del progetto High Luminosity - Large Hadron Collider include la progettazione di un nuovo sistema magnetico e 16 quadrupoli superconduttori inner triplet low-β devono essere sostituiti al fine di raggiungere un campo magnetico di picco di circa 12 T. Un così alto valore di campo magnetico rende necessario l'utilizzo di magneti superconduttori avvolti con cavi Rutherford in Nb_3Sn, al posto degli attuali in $NbTi$.

Il livello di quench di questi magneti (ovvero l'energia massima che il cavo può sopportare senza transire definitivamente allo stato normale) è un valore chiave per la protezione dalle perdite dovute al fascio, ed è prevedibile che sia significativamente diverso dai valori analizzati e misurati per magneti in $NbTi$ dell' LHC. In questo lavoro abbiamo applicato un modello numerico zero e mono-dimensionale di un cavo Rutherford multifilamentare dei magneti quadrupolari low-β, chiamati MQXF [1], per simulare le instabilità termo-elettriche durante un quench indotto dalle perdite del fascio. La deposizione di calore nel cavo superconduttore dovuta a tali perdite

è stata ottenuta attraverso computazioni eseguite con il codice FLUKA [2]. Per le proprietà materiali ed il modello superconduttivo è stata usata la parametrizzazione della superficie critica del Nb_3Sn usato ad ITER [3].

Nel modello zero-dimensionale, l'intero cavo è rappresentato da un singolo elemento termico caratterizzato da temperatura uniforme e proprietà termiche omogenee. Per queste analisi è stato utilizzato il codice CryoSoft ZERODEE [4].

Incrementando il livello di complessità del modello, si prendono in considerazione i domini termico, elettrico ed idraulico. Trascurando la sezione del cavo rispetto alla sua lunghezza, è possibile utilizzare un modello mono-dimensionale. La modellizzazione e le simulazioni sono state portare a termite attraverso il codice CryoSoft THEA [5][6], che permette non solo di analizzare i fenomeni termici di scambio di calore, ma anche la redistribuzione delle correnti tra i diversi filamenti e la fluido-dinamica dell' elio liquido che circonda il cavo. Per la parametrizzazione termica ed elettrica sono stati utilizzati i dati presentati in [7], mentre per lo scambio termico tra il bagno d'elio e il cavo si fa riferimento al modello empirico sviluppato da [8].

Per il codice THEA, sono stati effettuati numerosi studi di convergenza riguardanti il passo di integrazione temporale, la mesh e la tolleranza, con l'obiettivo di non perdere informazioni critiche durante le simulazioni.

Due diversi approcci allo studio del margine di stabilità sono stati effettuati: uno basato sull'analisi del singolo filamento ed un altro tenendo conto della totalità dei 40 filamenti dei quali è composto il cavo Rutherford. I risultati di questi due modelli sono stati confrontati al fine di determinare gli effetti di ridistribuzione di calore e corrente. Inoltre è stato studiato l'impatto dell'introduzione di un nucleo resistivo inserito tra i due strati del cavo Rutherford.

Gli andamenti delle temperature e delle correnti sono stati analizzati per ogni filamento, sia nello spazio che nel tempo, al fine comprendere meglio il comportamento del cavo durante la fase di quench o recovery.

Viene infine presentato un confronto tra i valori di quench ottenuti per un conduttore in Nb_3Sn nelle condizioni operative del quadrupolo inner triplet low-β (MQXF) di Hi-Lumi LHC, e quelli per un cavo Rutherford in $NbTi$ del quadrupolo (MQ) dell' LHC [9]. Sono state evidenziate le differenze e le analogie delle prestazioni di quench dei cavi impregnati per i magneti in Nb_3Sn e quelli non impregnati per i magneti in $NbTi$, nelle rispettive condizioni di lavoro.

Abstract

At CERN (European Organization for Nuclear Research), between 1998 and 2008, the world's largest and most powerful particle collider has been built. The LHC (Large Hadron Collider) is the biggest scientific instrument ever built to explore the new high-energy physic frontiers and it gathers a global user community of 7,000 scientists from all over 60 countries. The accelerated particles are made to collide together approaching the speed of light. This process allows to understand how the particles interact and provides insights into the fundamental laws of nature. After the latest amazing discoveries concerning the Higgs boson and the penta-quarks, another step forward is needed. To extend its discovery potential, the LHC will need a major upgrade around 2020 to increase its luminosity (rate of collisions) by a factor of 10 beyond the original design value (from 300 to 3000 fb^{-1}). As a highly complex and optimised machine, such an upgrade of the LHC must be carefully studied and requires about 10 years to implement. The scope of the Large Hadron Collider High Luminosity Project includes a new magnetic design and 16 superconducting inner triplet low-β quadrupoles have to be replaced to reach a magnetic peak field of about 12 T. Such a high value of magnetic field requires the use of superconducting magnets wound with Nb_3Sn Rutherford cables, instead of the actual ones made in $NbTi$.

The quench level of these magnets (i.e. the maximum energy that a cable can tolerate without quenching) is a key value required to set magnet protection from beam losses, and is expected to be significantly different from the computed and measured levels of the LHC $NbTi$ magnets. In this work, we applied both zero and one-dimensional numerical model of multi-strand Rutherford cables of the low-β quadrupole magnets, called MQXF [1], to simulate the electro-thermal instabilities of a beam-induced quench. The heat deposition on the superconducting cable due to the beam losses was obtained with computations performed with the FLUKA code [2]. For the material properties and superconducting model, the ITER Nb_3Sn critical surface parameterization has been used [3].

In the zero-dimensional model, the whole cable is lumped into a single thermal component characterised by uniform temperature and homogenised thermal properties. For thes analyses the CryoSoft ZERODEE [4] code has been used.

Increasing the level of complexity of the model, thermal, electric and hydraulic domains are taken into account. Neglecting the cable cross section in comparison with the longitudinal dimension, a one-dimensional model has been considered. The modelling and the simulations are carried out by means of the CryoSoft THEA [5][6] code, that allows to examine not only the thermal phenomena of heat exchange, but also the currents redistribution between different strands and the fluid-dynamic behaviour of the liquid Helium surrounding the cable. For the thermal and electric parameterization the data from [7] have been used, while for the heat exchange between the helium bath and the cable the empirical model presented in [8] is considered.

For the THEA code several studies of convergence concerning integration time steps, mesh and tolerance have been carried out, aiming not to lose critical information during the simulations.

Two kinds of investigation of the stability margin have been performed, one based on the analysis of the single strand, and the other accounting for all the 40 strands of the multi-strand Rutherford cable. The results of these two models are compared to analyse the effects of heat and current redistribution. The impact on quench energy of a resistive core embedded between the two layers of the Rutherford cables is also studied.

The trends of the temperatures and the currents are analysed for each strand both in the space and in the time, in order to better understand the behaviour of the cable during the quench or the recovery phase.

A comparison between the quench energy values obtained for the Nb_3Sn conductor in the working conditions of the Hi-Lumi LHC inner triplet low-β quadrupole (MQXF) and those of the $NbTi$ Rutherford cable of the LHC main quadrupole magnet (MQ) [9] is presented. The differences and similarities in quench performance between the impregnated cables for Nb_3Sn magnets and the non-impregnated ones for NbTi magnets at their respective typical working conditions in superconducting accelerator magnets are highlighted.

Contents

List of Figures **viii**

1 European Organization for Nuclear Research **1**

1.1 Large Hadron Collider - LHC 2

1.2 High Luminosity Large Hadron Collider HiLumi-LHC 3

2 Superconductivity **5**

2.1 Brief history of superconductivity 5

2.2 Superconducting properties 6

2.3 Stability 10

3 Nb_3Sn inner triplet - MQXF **15**

3.1 Design and magnetic field 15

3.2 Conductor characteristic 18

4 The 0-D Approach **20**

4.1 0-D model results 21

5 The 1-D Approach **24**

5.1 Thermal model 25

5.1.1 Heat exchange between strands 26

5.1.2 Heat exchange between strand and glass-epoxy 27

5.1.3 The heat exchange between glass-epoxy and Helium bath . . . 28

5.1.4 Thermal boundary and initial conditions 29

5.2 Hydraulic model 29

5.2.1 Hydraulic boundary and initial conditions 30

5.3 Electric model 31

5.3.1 Mutual and self-inductance . . . 32
5.3.2 Conductance calculation . . . 34
5.3.3 Electric boundary and initial conditions . . . 35
5.4 Magnetic field distribution . . . 35
5.5 Heat disturbance . . . 36
5.6 Temperature and Current distributions . . . 38

6 The 1-D model results **45**
6.1 Nb_3Sn and $NbTi$ cables comparison . . . 48
6.1.1 Stabiliser analysis - Copper . . . 52
6.1.2 Thermal conductivity analysis . . . 53
6.1.3 Distribution of the heat deposition . . . 54
6.1.4 Insulator analysis - Glass-epoxy . . . 54
6.2 Nb_3Sn cored cable . . . 57

7 Conclusion **60**

8 Appendix A - Convergence studies **61**
8.1 Integration time steps . . . 61
8.2 Thermal component . . . 62
8.2.1 Maximum integration time step . . . 62
8.2.2 Minimum integration time step . . . 64
8.3 Thermal and Electric components . . . 65
8.3.1 Maximum integration time step . . . 65
8.3.2 Minimum integration time step . . . 67
8.4 Tolerance . . . 69
8.5 Mesh dimension . . . 71
8.6 Error control . . . 72

9 Appendix B - Hitchhiker's guide to the Linux and LxPlus galaxy **75**

Bibliography **80**

List of Figures

1.1 Representation of the CERN accelerator chain 2

2.1 Historic plot of resistance versus temperature for mercury, from the 1911 Onnes experiment, shows the superconducting transition at 4.20 K. 6

2.2 Diagram of the Meissner-Ochsenfeld effect. Magnetic field lines, represented as arrows, are excluded from a superconductor when it is below its critical temperature. 7

2.3 Critical surface of $NbTi$, Nb_3Sn and Nb_3Ge in (T,B,J) space. 8

2.4 Comparison between the H-T diagram of type-I (a) and type-II (b) superconductor. 9

2.5 Two of the most severely damage interconnections in the LHC sector 3-4. 10

2.6 Spectrum of energy perturbations as a function of the characteristic time of energy deposition [10]. 11

2.7 An event tree for the evolution of an external energy input. The stability design and analysis are concentrated on the shaded area [10]. 12

2.8 The qualitative evolution of the temperature in a superconducting cable for an energy perturbation just below and just above the energy margin. 13

2.9 The location of the BLMs outside the cryostat in the LHC tunnel. . . 14

3.1 The MQXF real cross section. 16

3.2 The MQXF model cross section. The superconducting coils are highlighted in red. 17

3.3 Schematic of an accelerator dipole. 17

3.4 Magnetic flux density in the coil. 18

3.5 Nb_3Sn Rutherford cable for MQXF front view 18

3.6 Nb_3Sn Rutherford cable for MQXF cross section 19

4.1 Simple representation of the 0-D model 21
4.2 Quench energy of the MQXF inner layer middle-plane cable as a function of the heating time, with different values of current. 0-D model. 22
4.3 Comparison between the 0-D and 1-D models for high values of current. 22
4.4 Comparison between the 0-D and 1-D models for low values of transport current. 23

5.1 One-dimensional model overview 24
5.2 Thermal model representation 26
5.3 Heat exchange between strand and glass-epoxy representation 27
5.4 Electrical model representation 31
5.5 Representation of the strands numeration 33
5.6 Linear magnetic field function along different strands 35
5.7 Profile of the heat deposition along different strands 37
5.8 Profile of the temperature vs the heat disturbance of the first strands of a Nb_3Sn MQXF cable during the quench, induced by a heat disturbance of 10 μs. 39
5.9 Profile of the temperature vs the heat disturbance of the first strands of a $NbTi$ MQ cable during the quench, induced by a heat disturbance of 10 μs. 40
5.10 Profile of the temperature vs the applied magnetic field of the first strands of a Nb_3Sn MQXF cable during the quench, induced by a heat disturbance of 10 μs. 40
5.11 Profile of the temperature vs the applied magnetic field of the first strands of a $NbTi$ MQ cable during the quench, induced by a heat disturbance of 10 μs. 41
5.12 Profile of the current vs the heat disturbance field of the first strands of a Nb_3Sn MQXF cable during the quench, induced by a heat disturbance of 10 μs. 42
5.13 Profile of the current vs the heat disturbance field of the first strands of a $NbTi$ MQ cable during the quench, induced by a heat disturbance of 10 μs. 42

5.14 Profile of the current vs the applied magnetic field of the first strands of a Nb_3Sn MQXF cable during the quench, induced by a heat disturbance of 10 μs. 43
5.15 Profile of the current vs the applied magnetic field of the first strands of a $NbTi$ MQ cable during the quench, induced by a heat disturbance of 10 μs. 43

6.1 QXF Nb_3Sn: Quench energies vs. Heating time at different percentages of operating current $I_{op} = \frac{16.47}{40}$ kA, for the *1-strand* model. . . . 46
6.2 QXF Nb_3Sn: Quench energies vs. Heating time at the operating current $I_{op} = \frac{16.47}{40}$ kA, for the *1-strand* model with uniform (blue curve), non-uniform PEAK (red curve) and non-uniform MEAN (green curve) heat deposition. 46
6.3 QXF Nb_3Sn: Quench energies vs. Heating time at different percentages of operating current $I_{op} = 16.47$ kA, for the *40-strand* model with uniform (blue curves) and non-uniform PEAK (red curves) heat deposition. 47
6.4 QXF Nb_3Sn: Quench energies vs. Heating time at the operating current $I_{op} = 16.47$ kA, for the *40-strand* model with uniform (blue curve), non-uniform PEAK (red curve) and non-uniform MEAN (green curve) heat deposition. 47
6.5 Comparison between QXF Nb_3Sn and MQ $NbTi$ cables: Quench energies vs. Heating time at the operating current, for the *1-strand* model with non-uniform heat deposition. 50
6.6 Comparison between QXF Nb_3Sn and MQ $NbTi$ cables: Quench energies vs. Heating time at the operating current, for the *N-strand* model with non-uniform heat deposition 50
6.7 Comparison between *1-strand* and *36-strand* models for MQ $NbTi$ cable: Quench energies vs. Heating time at the operating current, with non-uniform heat deposition. 51
6.8 Comparison between *1-strand* and *40-strand* models for MQXF Nb_3Sn cable: Quench energies vs. Heating time at the operating current, with non-uniform heat deposition. 51

6.9 Comparison between different amounts of copper for the *1-strand* and the *40-strand* models for MQXF Nb_3Sn cable: Quench energies vs. Heating time at the operating current, with non-uniform heat deposition. 52
6.10 Comparison between different values of thermal conductivity for the *1-strand* and the *40-strand* models for MQXF Nb_3Sn cable: Quench energies vs. Heating time at the operating current, with non-uniform heat deposition. 53
6.11 MQ $NbTi$: Quench energies vs. Heating time at the operating current , for the *36-strand* model with uniform (blue curve), non-uniform PEAK (red curve) and non-uniform MEAN (green curve) heat deposition. 54
6.12 Comparison between the presence and the absence of interstitial helium, replaced with glass-epoxy, for the *1-strand* model for MQ $NbTi$ cable: Quench energies vs. Heating time at the operating current, with non-uniform heat deposition. 55
6.13 Comparison between the presence and the absence of interstitial helium, replaced with glass-epoxy, for the *36-strand* model for MQ $NbTi$ cable: Quench energies vs. Heating time at the operating current, with non-uniform heat deposition. 56
6.14 Comparison between different values of glass-epoxy area for the *40-strand* model for QXF Nb_3Sn cable: Quench energies vs. Heating time at the operating current, with non-uniform heat deposition. . . . 56
6.15 Representation of the 1-D cored model. 57
6.16 Comparison between cored and non-cored QXF Nb_3Sn cable at 100% of operating current : Quench energies vs. Heating time at the operating current, with non-uniform heat deposition. 58
6.17 Comparison between cored and non-cored QXF Nb_3Sn cable at 25% of operating current : Quench energies vs. Heating time at the operating current, with non-uniform heat deposition. 58
6.18 Comparison between non-cored and cored with and without the core heat capacity: Quench energies vs. Heating time at the operating current, with non-uniform heat deposition. 59

8.1 Stability of the Minimum Quench Energy in terms of maximum integration time steps. [Thermal component] 63

8.2 Minimum Quench Energy as a function of heat disturbance duration, with different maximum integration time steps. [Thermal component] 63
8.3 Stability of the Minimum Quench Energy in terms of minimum integration time steps. [Thermal component] 64
8.4 Minimum Quench Energy as a function of heat disturbance duration, with different minimum integration time steps. [Thermal component] 65
8.5 Stability of the Minimum Quench Energy in terms of maximum integration time steps. [Thermal and electric components] 66
8.6 Minimum Quench Energy as a function of heat disturbance duration, with different maximum integration time steps. [Thermal and electric components] 66
8.7 Stability of the Minimum Quench Energy in terms of minimum integration time steps. [Thermal and electric components] 67
8.8 Minimum Quench Energy as a function of heat disturbance duration, with different minimum integration time steps. [Thermal and electric components] 68
8.9 Stability of the Minimum Quench Energy in terms of tolerance. [Thermal component] 69
8.10 Stability of the Minimum Quench Energy in terms of tolerance. [Thermal and electric components] 70
8.11 Stability of the Minimum Quench Energy in terms of mesh element number . [Thermal component] 71
8.12 Stability of the Minimum Quench Energy in terms of mesh element number for long heat disturbance . [Thermal and Electric components] 72
8.13 Stability of the Minimum Quench Energy in terms of error control. [Thermal component] 73
8.14 Stability of the Minimum Quench Energy in terms of error control. [Thermal and electric components] 74

1. European Organization for Nuclear Research

"At CERN, the European Organization for Nuclear Research, physicists and engineers are probing the fundamental structure of the universe. They use the world's largest and most complex scientific instruments to study the basic constituents of matter - the fundamental particles. The particles are made to collide together at close to the speed of light. The process gives the physicists clues about how the particles interact, and provides insights into the fundamental laws of nature" [11]. Established in 1954, located in Geneva - Switzerland, nowadays it is the the largest particle physics laboratory ever built. It counts 22 member states and co-operations with almost every state in the world. Birthplace of the World Wide Web, it has accomplished many scientific achievements, last of them the discovery of the Higgs boson (Nobel prize in 2013) and the penta-quarks (2015). CERN is not only one of the most important research centre of the world, but it also represent the joint of diverse cultures and languages, the hard work and the passion over the differences. A virtuous and peaceful example of international collaboration with an unique aim: Science.

1.1 Large Hadron Collider - LHC

"The Large Hadron Collider (LHC) is the world's largest and most powerful particle accelerator. It first started up on 10 September 2008, and remains the latest addition to CERN's accelerator complex. The LHC consists of a 27-kilometre ring of superconducting magnets with a number of accelerating structures to boost the energy of the particles along the way"[11]. Through the complex system of accelerator, shown in *Fig. 1.1* the particle beams can reach the record energy of 6.5 TeV per beam (May 2015):

- Linac 2 accelerates the protons to the energy of 50 MeV
- Proton Synchrotron Booster (PSB) accelerates the protons to energy of 1.4 GeV
- Proton Synchrotron (PS)accelerates the protons to the energy of 25 GeV
- Super Proton Synchrotron (SPS) accelerates the protons to the energy of 450 GeV
- Large Hadron Collider (LHC) accelerates the protons to the energy of 6.5 TeV

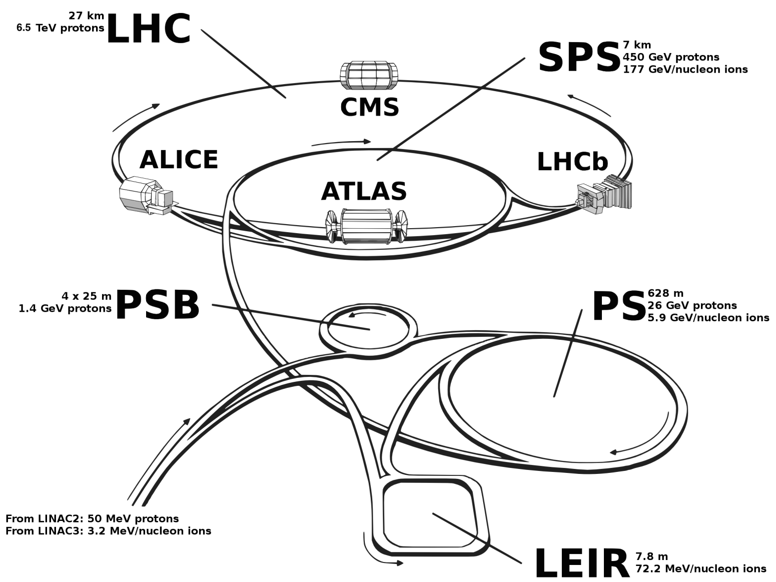

Figure 1.1 Representation of the CERN accelerator chain

In order to provide the magnetic fields, necessary to the bending and the confinement of the beam, 1600 superconducting magnets are installed and over 95 tonnes of liquid Helium are needed to maintain the system at the operating temperature of 1.9 K (-271.25°C) The particles travel inside the pipes, in opposite directions, with a velocity equal to the 99,9999991% of the speed of light. The energies are so high that the collision between the two beams is able to reproduce the characteristics of the first instants of the universe after the Big Bang. To modify the particles velocity ($\mathbf{v}$) and trajectory, the electric ($\mathbf{E}$) and the magnetic ($\mathbf{B}$) fields have to be used:

$$\mathbf{F} = q(\mathbf{E} + \mathbf{v} \times \mathbf{B}) \tag{1.1}$$

where $\mathbf{F}$ is the electromagnetic force and q the charge of the particle. Therefore, in the LHC tunnel there are three main elements:

- Radio Frequency (RF) cavities increase the particle energy at every turn, based on an alternating electrical potential which acts on the particles as an accelerating field
- Dipole Magnets (MB) generate the magnetic field able to bend the particle beam, maintaining it in the reference trajectory
- Quadrupole Magnets (MQ) focus or defocus the particles onto the reference orbit, preventing them from diverging from the center of the beam pipe

Through the detectors, ALICE, ATLAS and CMS, it is possible to trace and analyse the particles generated by the high energies impacts.

1.2 High Luminosity Large Hadron Collider HiLumi-LHC

In scattering theory and accelerator physics, luminosity (L) is the ratio of the number of events detected (N) in a certain time (t) to the interaction cross-section (σ) [12]:

$$L = \frac{1}{\sigma}\frac{dN}{dt} \tag{1.2}$$

The aim of the HiLumi project is to introduce the necessary changes in the LHC to increase its luminosity by a factor ten, from 300 to 3000 fb^{-1}, providing a better chance to see rare processes and improving statistically marginal measurements. With this kind of upgrade, the LHC will push the limits of human knowledge, enabling physicists to go beyond the Standard Model and its Higgs boson. Exiting and unknown phenomena, like dark matter and the supersymmetry, could be studied and analysed, opening the doors to unbelievable improvement in science and technology. CERN will devote 950 million CHF of its budget over a period of 10 years to the development of the High-Luminosity LHC.

"But upgrading such a large scale, complex piece of machinery is a challenging procedure that will take a decade to complete. The process hinges on a number of innovative technologies [...] cutting-edge 11-13T superconducting magnets, compact and ultra-precise superconducting radio-frequency cavities for beam rotation, as well as 300-m-long, high-power superconducting links with zero energy dissipation" [11].

A key factor is the development of the new magnetic system. Among the magnets that will be replaced are the 16 superconducting inner triplet low-β quadrupole, the so called MQXF, placed in proximity of the ATLAS and CMS detectors. Due to the high values of the magnetic field (about 12 T), it will be necessary the use of the Nb_3Sn superconducting coils, instead of the actual $NbTi$ magnets. The quench level of these magnets (i.e. the maximum energy that a cable can tolerate without quenching) is a fundamental value required to set magnet protection from beam losses, and is expected to be significantly different from the computed and measured levels of the LHC Nb-Ti magnets.

2. Superconductivity

2.1 Brief history of superconductivity

On the 10th of July 1908, Heike Kamerlingh Onnes, professor at the Leiden University, produced for the first time liquefied helium, reaching the temperature of 4.2 K (-269 °C). After three years he noted *"Kwik nagenoeg nul"* : Quick [silver] near-enough null. Analysing the behaviour of the electrical resistance at cryogenic temperature he noticed that: *"Mercury has passed into a new state, which on account of its extraordinary electrical properties, may be called the superconducting state"* [13] characterised by a not measurable value of electrical resistance as shown *Fig. 2.1*. This transition occur under a critical temperature Tc, different for each material.

The next milestone occurred in 1933 when Meissner and Ochsenfeld discovered that a material in superconducting state expels the magnetic field, becoming a perfect diamagnetic material [14]. The first phenomenological theory of superconductivity ables to explain the Maissner effect, was developed by the London brothers in 1935, through the formulation of the weel-known London's equations [15].

A quantum explanation was proposed in 1957 by Bardeen, Cooper and Schrieffer: the so-called BCS theory [16]. In 1962, the first commercial superconducting wire, a niobium-titanium alloy, was developed by researchers at Westinghouse, allowing the construction of the first practical superconducting magnet. In 1986 it was discovered the superconductivity in a lanthanum-based cuprate perovskite material, with a transition temperature of 35 K [17]. Just a year later, replacing the lanthanum with yttrium (YBCO), the critical temperature of 92 K was reached [18]. In 2001 these particular properties have been discovered in magnesium diboride (MgB_2), that has proven to be an inexpensive and useful superconducting material with a critical temperature of 35 K [19].

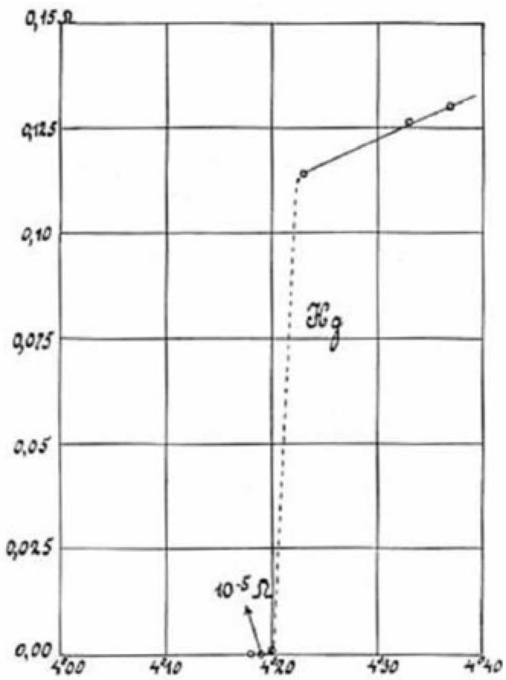

Figure 2.1 Historic plot of resistance versus temperature for mercury, from the 1911 Onnes experiment, shows the superconducting transition at 4.20 K.

2.2 Superconducting properties

Superconductivity is a remarkable phenomenon whereby certain materials, when cooled to very low temperatures, become excellent conductors of electricity. Unlike the gradual change of the electrical resistance with temperature in common metals, the superconducting state appears quite abruptly at the critical temperature Tc, which is a characteristic parameter of the specific metal. Below this temperature the resistance is not just very small; as far as it can be seen from the results of some very sensitive experiments, it is absolutely equal to zero. The vanishing resistance is not enough to define a material as a superconductor because every conductor, at temperature close to the absolute zero, tends towards a null value of resistance. Superconductors exhibit a perfect diamagnetism below the critical temperature Tc, ejecting external applied magnetic field by means of superficial super-currents, until the limit value of the critical magnetic field Bc. This phenomenon is called Meissner-Ochsenfeld effect *Fig. 2.2*.

The classical model of superconductivity, developed by the London brothers in

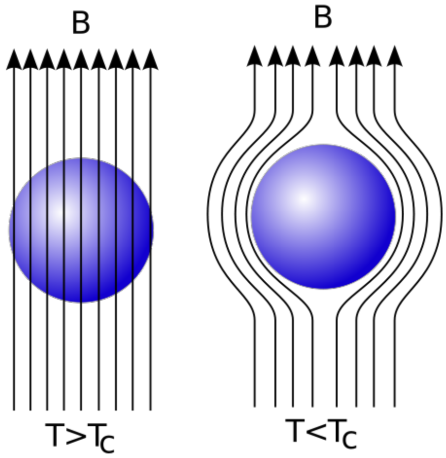

Figure 2.2 Diagram of the Meissner-Ochsenfeld effect. Magnetic field lines, represented as arrows, are excluded from a superconductor when it is below its critical temperature.

1935 [15], can explain these two basic characteristics of the superconductors through the following equations. This model does not take into account quantum phenomena e does not allow the existence of the fluxons.

$$
\begin{aligned}
&\mathbf{E} = \mu_0 \lambda^2 \frac{\partial \mathbf{J}}{\partial t} && \Rightarrow && \text{null resistivity} \\
&\mu_0 \lambda^2 \nabla \times \mathbf{J} = -\mathbf{B} && \Rightarrow && \text{Meissner-Ochsenfeld effect}
\end{aligned}
$$

Another critical parameter of superconductivity is the critical current density that a material can carry without exhibit a transition to the normal state. Unlike the critical temperature and the magnetic field, the critical current is not a intrinsic feature of the material, but it is depend on the thermal and mechanical treatment induced in the cable. These three properties are related to each other by the critical surface in (T,B,J) space, which is characteristic of the considered material *Fig. 2.3*. Superconductivity prevails everywhere below this surface, with normal resistivity everywhere above it.

Depending on the magnetic behaviour, superconductors are classified in two categories: type-I and type-II. Several elements present a type-I superconductivity and exhibit the properties explained above. Type-II superconductors are typically alloys and compounds, and they present a gradual transition the the normal state across a region of *mixed state* behaviour. Above the lower critical magnetic field H_{c1}, magnetic vortices penetrate inside the material and induced a local transition to the normal state. The quantum mechanics imposes that each vortex carries a quantum of magnetic flux, called fluxon. The vortex density increases with increasing field strength until the upper critical magnetic field H_{c2}, where the complete transition to the normal state occurs *Fig. 2.4*.

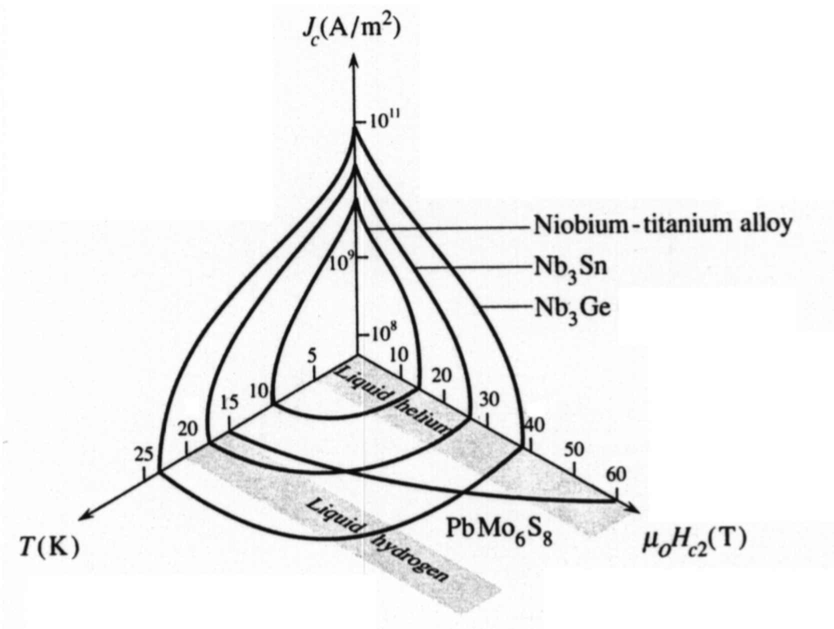

Figure 2.3 Critical surface of $NbTi$, Nb_3Sn and Nb_3Ge in (T,B,J) space.

The critical magnetic field of the type-I superconductors has an extremely low value, hence this kind of material does not have any practical applications. The H_{c2} field of type-II superconductors can reach interesting values of tens of Tesla. Concerning technical operations, superconductors always work in the mixed state, in absence of perfect diamagnetism, characterised by the existence of quantized magnetic flux vortex inside the material. The presence and relative motion of these vortex, by means of the Lorentz's forces, induce, especially when subjected to AC current/field, dissipations and losses.

As already said, some materials exhibits superconducting properties if operating below a critical temperature Tc. A different kind of superconductors classification can be done, based on this intrinsic feature. Low Temperature Superconductors are metallic materials with a critical temperature value below the 30-40 K, whose prop-

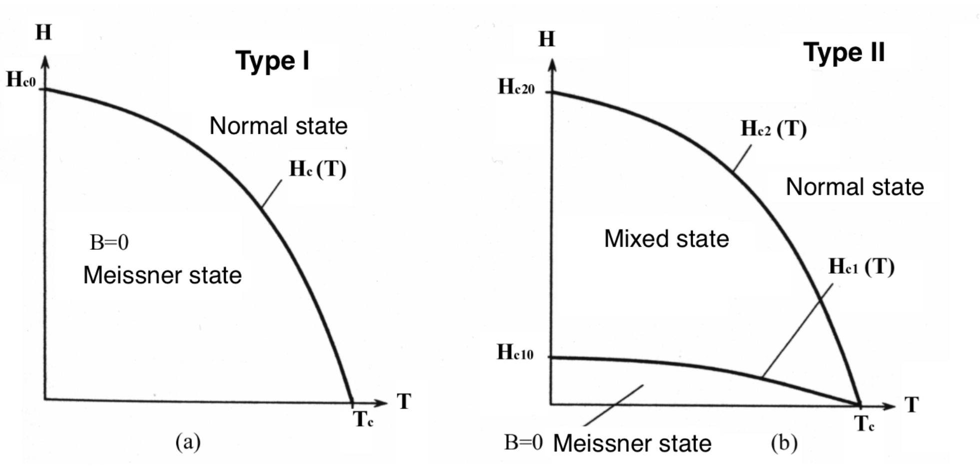

Figure 2.4 Comparison between the H-T diagram of type-I (a) and type-II (b) superconductor.

erties can be explained through the BCS theory [16]. This quantum theory analyse the superconducting phenomena introducing the so-called *Cooper pairs*: two electrons, linked by a electron-phonon coupling, can flow through the crystal lattice without interaction and consequent loss of energy. In the 1986 a new kind a superconductors, based on copper oxide layers CuO_2, has been discovered. These ceramic materials do not follow the BCS theory and exhibit very high values of critical temperature (90-100 K). They can be called High Temperature Superconductors. Of course the HTS open the doors to new applications of the superconductivity, restricted until that moment by prohibitive temperature and cooling. The possibility of using liquid Nitrogen, instead of Hydrogen or Helium, abruptly reduces the operating cost. However, HTS superconductors like $Bi_2Sr_2CaCu_2O_8$ (first generation) and $YBa_2Cu_3O_7$ (second generation) are characterised by complex manufacturing and substantial costs. An "hybrid" material is the magnesium diboride (MgB_2), that is a BCS superconductor with a critical temperature of 39 K. It is obtained by common and cheap material and has strong and feasible possibilities of implementation in several fields, like the current leads for the LHC or HVDC cable for electric transmission through the grid.

The analyses carried out in this dissertation are focussed on $NbTi$ and Nb_3Sn, both type-II LTS superconductors operating at the temperature of super-fluid liquid Helium of 1.9 K. It is no difficult to understand that, at this demanding condition, every heat perturbation and unwanted temperature oscillation can compromise irreversibly the whole system. Unexpected transition to the normal state can not only destroy the magnets, but it can also induce the evaporation of the Helium, producing catastrophic events at the structural level of the LHC. It is essential to understand how heat perturbations can affect the superconducting coils and especially how they react in terms of temperature and currents.

2.3 Stability

Control and prevention of the transition from superconducting state to the normal one, *quench*, is one of the most important and thorny problem concerning this technology. In 2008, during powering tests of the main dipole circuit of the LHC, a fault occurred in the electrical bus connection in the region between a dipole and a quadrupole, resulting in huge release of energy, increase of the vaporised helium pressure and consequent relevant mechanical damages as shown in *Fig. 2.5.* The total cost of the incident has been estimated in about 16 millions of euros.

Figure 2.5 Two of the most severely damage interconnections in the LHC sector 3-4.

"A principle not yet fully understood at the time was that of stability of the

cable with respect to external disturbances. Insufficient stability and large external disturbances were the key issues in the failure of the early experiments on superconducting magnets. It has since become understood that a superconducting magnet is always subject to a series of energy inputs of very different natures, time-scales, and magnitudes, the so-called disturbance spectrum" [10] *Fig. 2.6.*

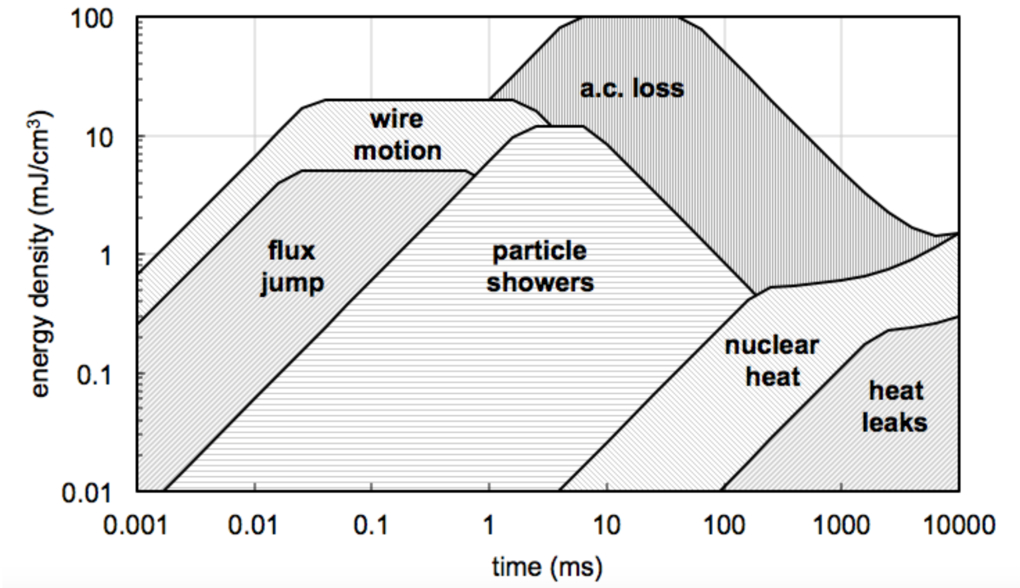

Figure 2.6 Spectrum of energy perturbations as a function of the characteristic time of energy deposition [10].

At cryogenic temperatures almost all the materials have a small heat capacity, and the difference between the operating temperature T_{op} and the temperature at which current sharing starts T_{cs} must be kept small for reason of costs. The energy introduction and the consequent temperature increase can be sufficient to take the superconducting material above the critical conditions, inducing a normal zone propagation and Joule heating generation. If not prevented by other mechanisms, the temperature in the normal zone increases and the normal front propagates, inducing an irreversible thermal runaway process that lead the complete loss of superconductivity in the magnet: a quench *Fig. 2.7.*

The *stability margin* is the minimum energy density that an external source needs to provide to the cable to cause a thermal runaway. A relevant source of disturbance in the operation of an accelerator magnet is the heat released on the superconducting wires by the losses due to the shower of secondary particles generated by particles lost from the beam [9]. The impact of protons with magnet components

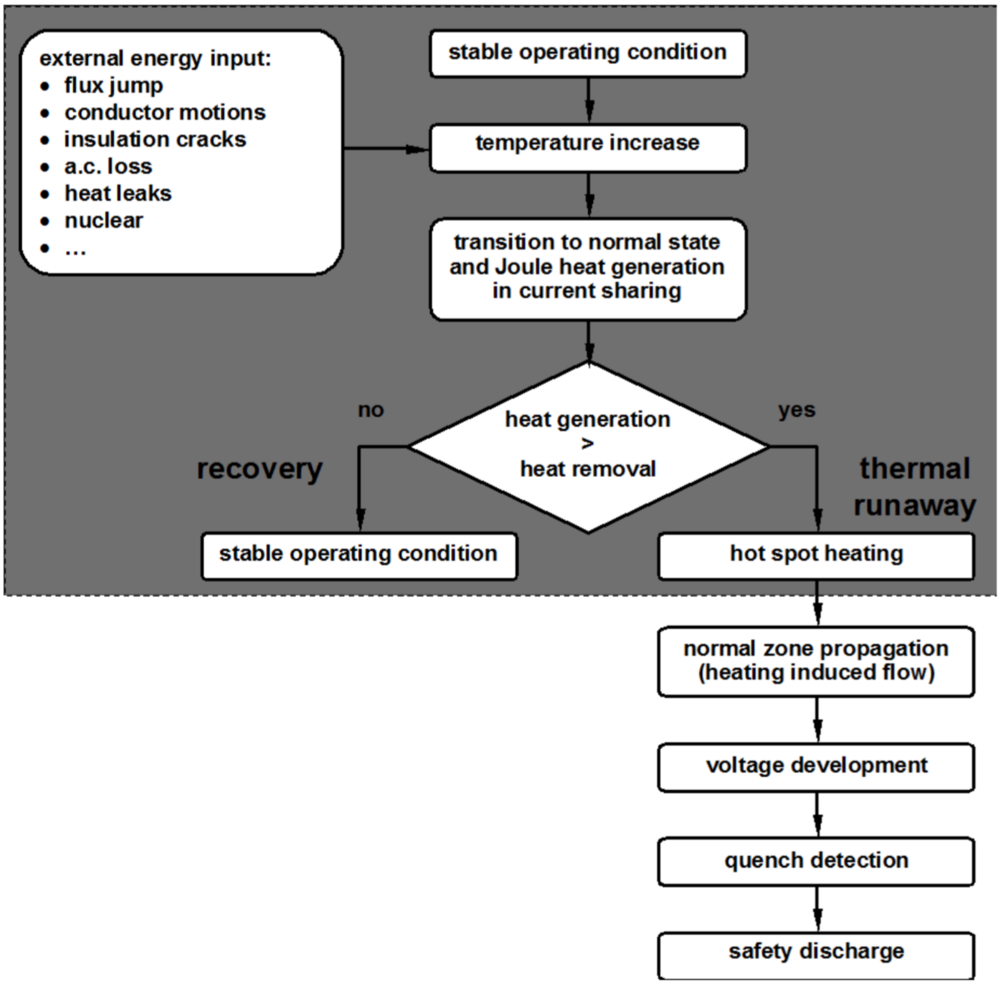

Figure 2.7 An event tree for the evolution of an external energy input. The stability design and analysis are concentrated on the shaded area [10].

produces a flux of secondary particles that is measured by Beam Loss Monitors installed outside the magnet cryostats [20]. The modelization of this particular kind of losses is presented in the section 5.5.

The evolution of the temperature is governed by a transient heat balance, explained in the section 5.1, containing the following term:

- external heat perturbation
- Joule heating generation
- heat capacity - enthalpy of the cable
- heat conduction along the cable and through the different strands
- heat exchange with the coolant

The combination of these five factors allows to determine the evolution of the system and the possibility of quench or recovery *Fig. 2.8*

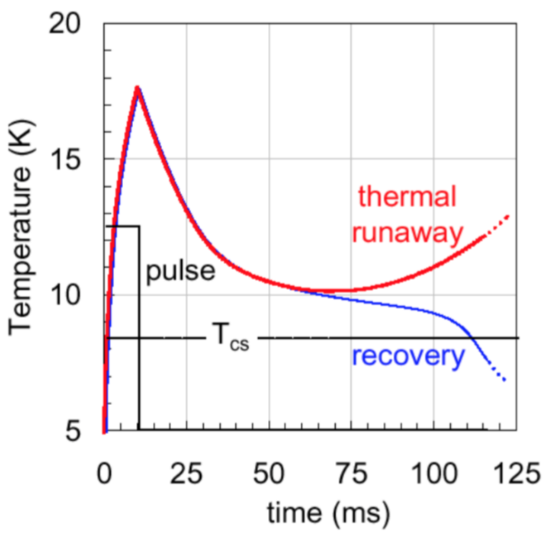

Figure 2.8 The qualitative evolution of the temperature in a superconducting cable for an energy perturbation just below and just above the energy margin.

A protection system, called Beam Loss Monitoring System *Fig. 2.9*, has been installed around the ring to monitor the lost particles and take corrective actions in case of the beam losses exceeds a threshold. The aim of this system is to predict a beam induced quench and dump the beam, avoiding destructive phenomena concerning the not controlled quenching of the magnets. The effective value of the quench limits is essential for the efficient operation of the BLMs, hence of the LHC. Several studies have been carried out about the calculation of the quench limits, however a complete and accurate analysis of these phenomena is extremely complicated and even today the values of the stability margins for the LHC superconducting magnets are affected by substantial uncertainties.

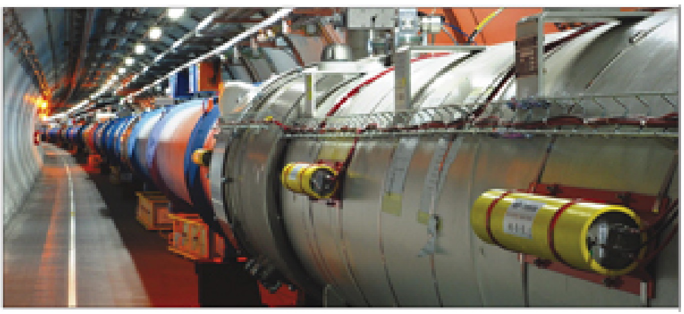

Figure 2.9 The location of the BLMs outside the cryostat in the LHC tunnel.

According with [21] three main regimes can be distinguished in the study of the thermal behaviour of $NbTi$ cables subjected to beam losses:

- short duration of losses [$< 1ms$]: the quench limit is determined by the enthalpy margin of the cable, without contribution from liquid helium
- intermediate duration of losses [$1ms-1s$]: the interstitial helium plays a crucial role because of its large heat capacity
- stady-state losses [$> 1s$]: the heat is constantly removed with a rate determined by the thermal properties of the cable insulation

The most recent and detailed analysis for the beam-induced quench level of the LHC has been performed through a "pseudo-experimental" approach presented in [22], based on the reconstruction of the energy introduced in the magnet at quench by means of the Beam Loss Monitors and FLUKA simulations [2].

3. Nb_3Sn inner triplet - MQXF

"The High Luminosity LHC (HL-LHC) project is aimed at implementing the necessary changes in the LHC to increase its integrated luminosity by a factor ten. Among the magnets that will be replaced are the 16 superconducting inner triplet (low-β) quadrupoles placed around the two high luminosity interaction regions (ATLAS and CMS experiments) [...] The resulting conductor peak field of about 12 T will require the use of Nb_3Sn superconducting coils. We present in this document the design HL-LHC low-β quadrupole magnets, called MQXF, focusing in particular on superconductor characteristics, coil lay-out, support structure concept, and quench protection system." [1]

3.1 Design and magnetic field

"The first function of a (superconducting) magnet is to guide and steer the particle, i.e. to keep it in orbit in a circular accelerator or to just bend in a transfer line. The second main function is focusing the beam, thus providing it with the necessary stability in the plane perpendicular to the trajectory" [23].

The aim of the HiLumi-LHC low-β quadrupole magnets is to collimate the beam, in order to optimise its intensity and dimension. A cross section of the MQXF is shown in *Fig. 3.1* and *Fig. 3.2*, where the superconducting coils are highlighted in red. In contrast to classical electromagnets, the field in a superconducting accelerator magnet is mainly produced by the current in the conductor. Very schematically, these particular kind of magnets for large scale accelerators consist of a coil wound, with characteristic racetrack configuration as shown in*Fig. 3.3*, around the bore which delimits the vacuum chamber hosting the beam.The large Lorentz forces that are experienced by the coil (hundreds of tons per meter) cannot be reacted by the winding alone and hence the force is transferred to a structure that guarantees mechanical stability and rigidity. The iron yoke that surrounds this assembly closes the magnetic circuit, shielding the surroundings from stray fields and providing a marginal gain of magnetic field in the bore. In addition, it can have a structural function in reacting or transferring the Lorentz forces from the coil to an external cylinder. Finally, the magnet is enclosed in a cryostat that provides the thermal barrier features necessary for cooling the magnet to the operating temperature.

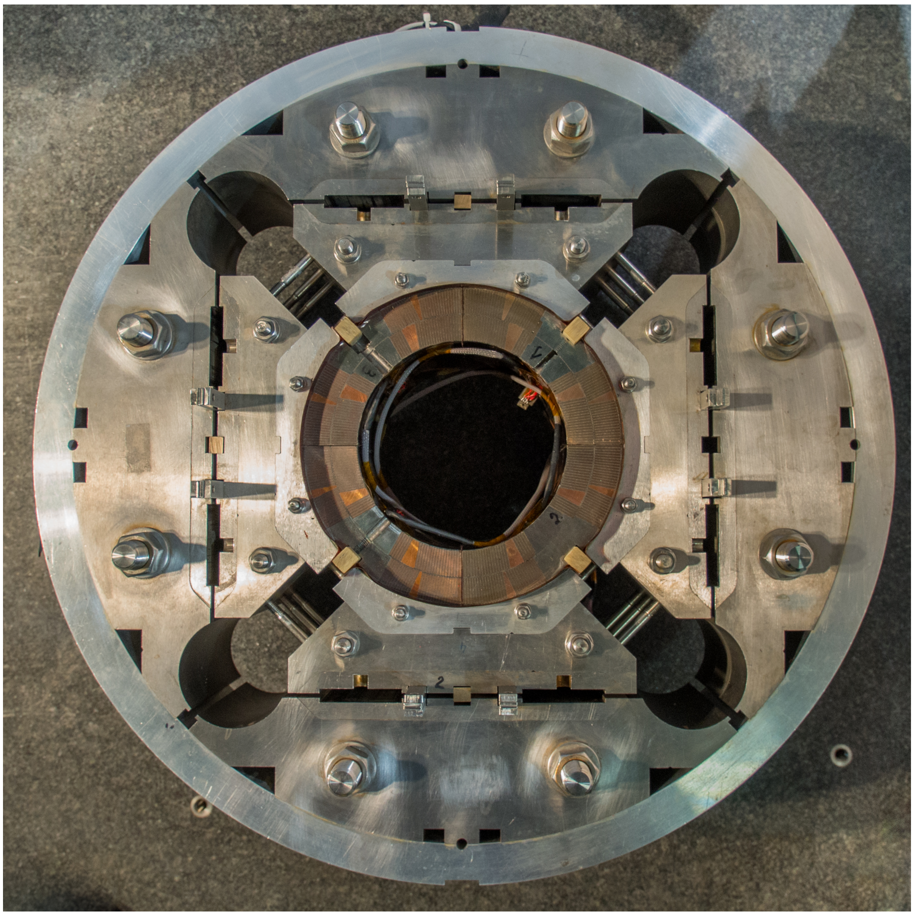

Figure 3.1 The MQXF real cross section.

In *Fig. 3.4* the magnetic field density in the coil at nominal current is plotted. At nominal current the peak field in the coil reaches 11.42 T. The analyses of this dissertation in focussed on the middle-plane inner layer cable. As *Fig. 3.4* the magnetic field along the cable is strongly variable: 9.78 T to 2.42 T at the nominal current of 16470 A [24]. The simulations have been performed using the hypothesis of linear magnetic field variation, as better explained in 5.4.

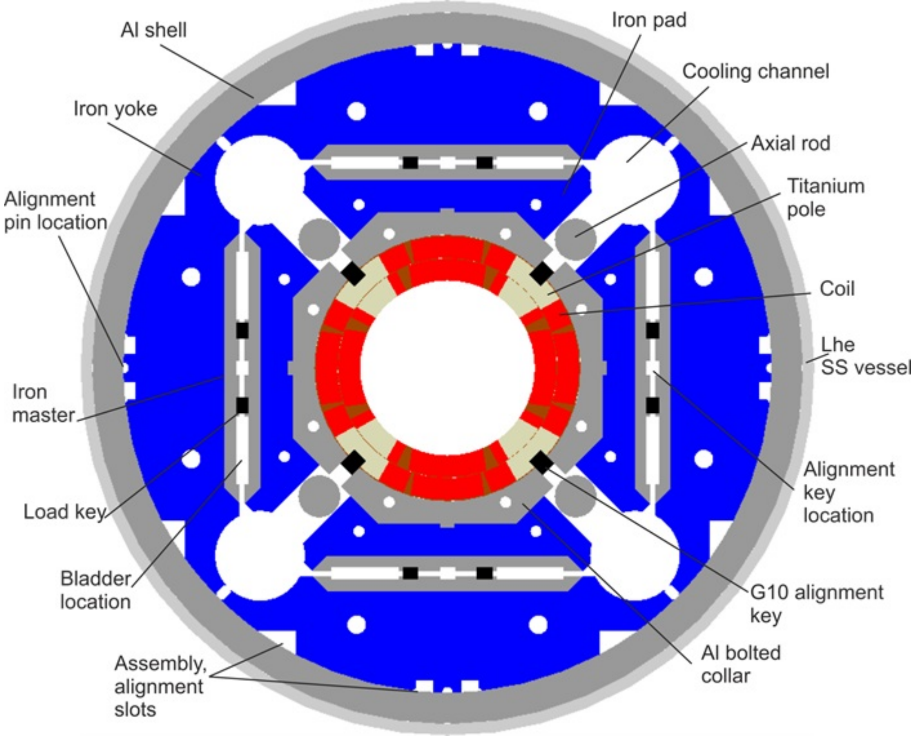

Figure 3.2 The MQXF model cross section. The superconducting coils are highlighted in red.

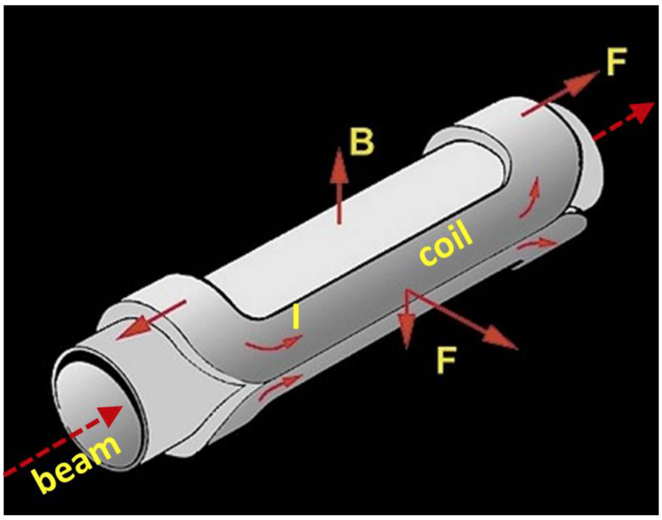

Figure 3.3 Schematic of an accelerator dipole.

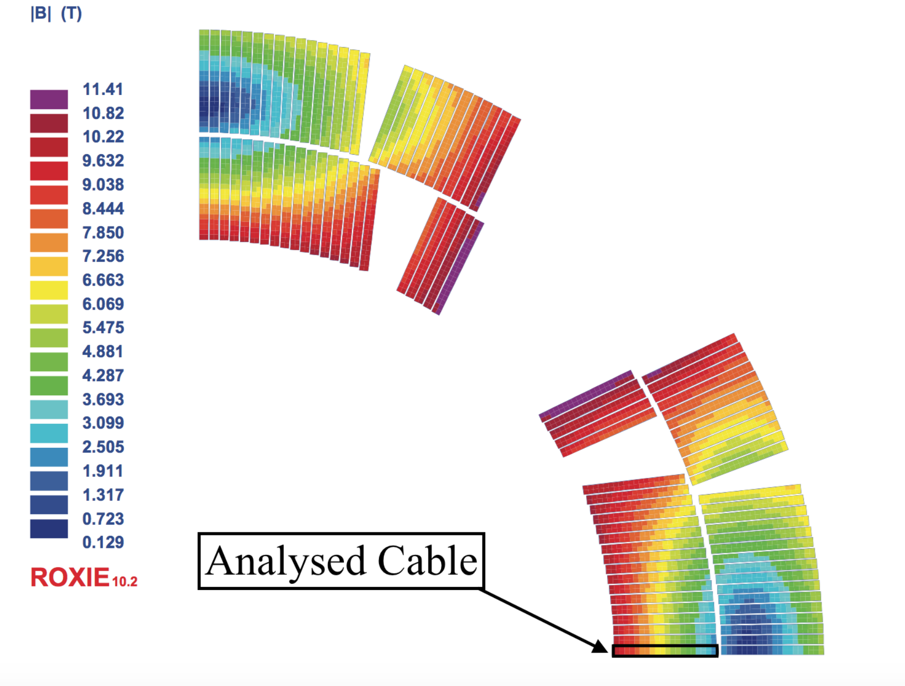

Figure 3.4 Magnetic flux density in the coil.

3.2 Conductor characteristic

The superconducting coils are composed by Nb_3Sn Rutherford cables. As the *Fig. 3.5* and the *Fig. 3.6* show, the cable is made of 40 twisted strands. This means that each strand follows a non-straight path, and consequently it is subjected to a non-uniform heat deposition and magnetic field, as explained in the sections 5.4 and 5.5.

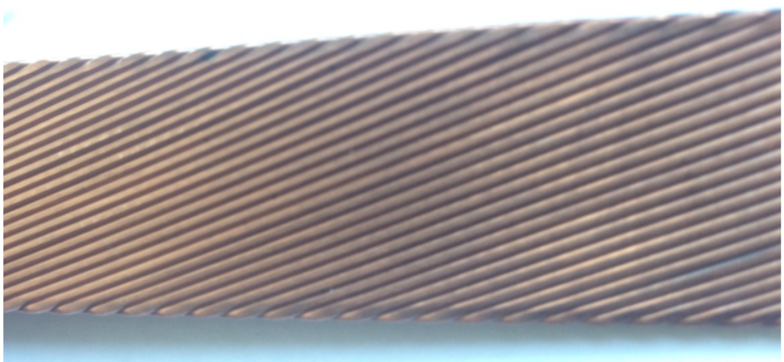

Figure 3.5 Nb_3Sn Rutherford cable for MQXF front view

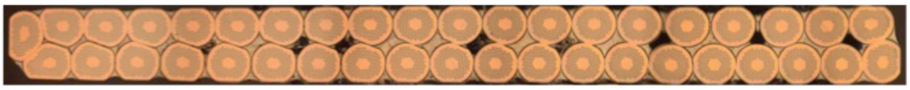

Figure 3.6 Nb_3Sn Rutherford cable for MQXF cross section

The main geometric parameters of the cable and its nominal operating condition are illustrated in *Table 3.1.*

MQXF v2 cable parameters		
Cable Data		
Cable mid-thickness	[mm]	1.525
Keystone angle	[deg]	0.4
Cable width	[mm]	18.15
Insulator thickness	[mm]	0.145
Number of strands		40
Strand diameter	[mm]	0.850
Cu/NonCu		1.20
Transposition pitch	[mm]	109
Operating Parameters		
Peak Field	[T]	11.4
Current	[kA]	16.47
Temperature	[K]	1.9

Table 3.1 MQXF geometrical and operating parameters

The strands are surrounded by a glass fiber insulator, *Glass-Epoxy*. It is important to highlight that, differently from the $NbTi$ cables, Nb_3Sn coils are impregnated with epoxy resin. The resin fills the spaces between strands and prevents the penetration of the interstitial helium. Therefore there is no internal cooling in the cable, and the heat occurs through the epoxy glass and the resin. This insulating configuration implies a drastic reduction of the stability margin, especially at fast time scale.

4. The 0-D Approach

Neglecting the longitudinal cable dimensions, the details of the helium flow and the current distribution, a Zero-Dimentional model can be applied to describe the electro-thermal transients occurring at quench. Moreover, the strands in the cable cross-section are lumped into a single thermal component characterised by uniform temperature and homogenised thermal properties. For this kind of analysis the *ZERODEE* Software [4] has been used. The cable, the insulator and the Helium bath are taken into account as three different elements and the set of equations solved by the program is the following:

$$A_{St}C_{St}\frac{dT_{St}}{dt} = \dot{q}'_{St} + \dot{q}'_{Joule} - p_{St,He}h_{St,He}(T_{St} - T_{He}) - p_{St,Ja}h_{St,Ja}(T_{st} - T_{Ja}) \tag{4.1a}$$

$$A_{Ja}C_{Ja}\frac{dT_{Ja}}{dt} = -p_{Ja,He}h_{Ja,He}(T_{Ja} - T_{He}) - p_{St,Ja}h_{St,Ja}(T_{Ja} - T_{St}) \tag{4.1b}$$

$$A_{He}C_{He}\frac{dT_{He}}{dt} = -p_{St,He}h_{St,He}(T_{St} - T_{He}) - p_{Ja,He}h_{Ja,He}(T_{Ja} - T_{He}) \tag{4.1c}$$

List of symbols used in the *(4.1)* equation		
A_i	$[m^2]$	cross section of the i-th component
ρ_i	$[Kg/m^3]$	density of the i-th component
C_i	$[J/KgK]$	specific heat of the i-th component
T_i	$[K]$	temperature of the i-th component
$\dot{q}'_{St}$	$[W/m]$	external heat input per unit lenght
$\dot{q}'_{Joule}$	$[W/m]$	generated Joule power per unit leght
p_{ij}	$[m]$	contact perimeter between the i-th and the j-th component
h_{ij}	$[W/m^2K]$	heat transfer coefficient between the i-th and the j-th component

Table 4.1 List of symbols used in the *(4.1)* equation

where the subscripts refer to the strands (St), jacket (Ja) or helium (He) in the conductor. The three components, with cross section A, have heat capacities C that are computed for each cable component as the sum of stabiliser and superconductor (strands), steel and insulator (jacket), and the Helium bath cross section. The non-uniformity of the heat deposition and the magnetic field along the longitudinal coordinate are not taken into account. A simple representation of the model is shown in *Fig. 4.1.* Is important to underline that the heat exchange between the strands and the Helium bath can only occur through the glass-epoxy: in other words, there is NO direct contact between the Helium bath and the strands.

Figure 4.1 Simple representation of the 0-D model

4.1 0-D model results

The results, for different levels of transport current, are shown in *Fig. 4.2.* It is important to note that the values of magnetic field vary with the current percentage, as shown in *Table 5.6.* As stressed above, the non-uniformity of the magnetic field and the heat deposition cannot take into account, and the B_{max} and the peak value of heat disturbance have been chosen for the simulations. Obviously the stability of the cable is inversely proportional to the current density and, as expected, lower values of current determine higher quench energies.

Furthermore these values do not exhibit a significant variation with increasing the heating time. The validation test with the 1-D model is presented in the *Fig. 4.3* and *Fig. 4.4*, and it exhibits a very good agreement between the 0-D and 1-D models both for high and low currents.

This implies that, for uniform heat deposition and magnetic field, a zero-dimensional model can be used without losing any important information about the analysed system. Of course, the usage of such a simple model allows to save a huge

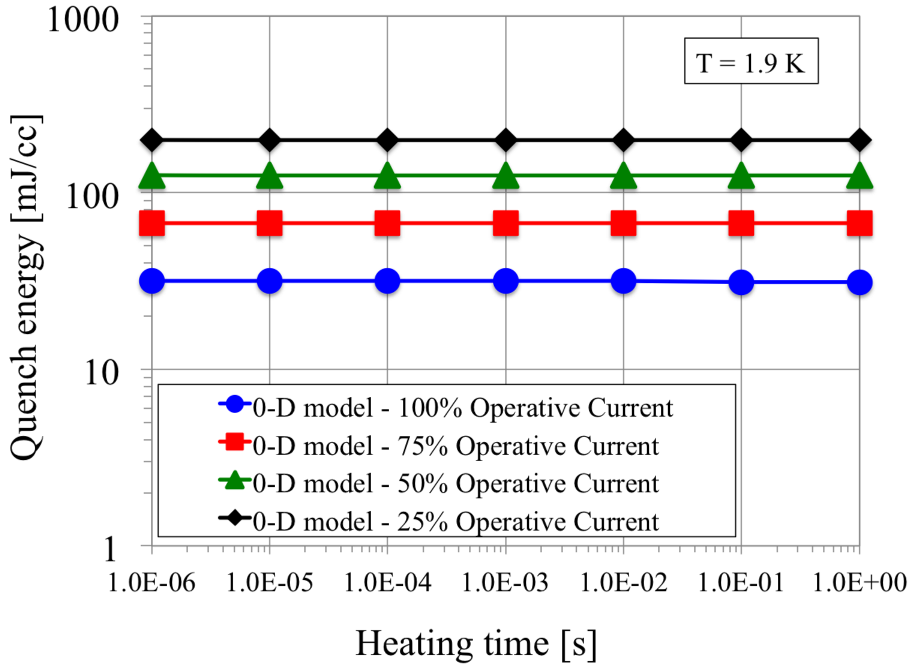

Figure 4.2 Quench energy of the MQXF inner layer middle-plane cable as a function of the heating time, with different values of current. 0-D model.

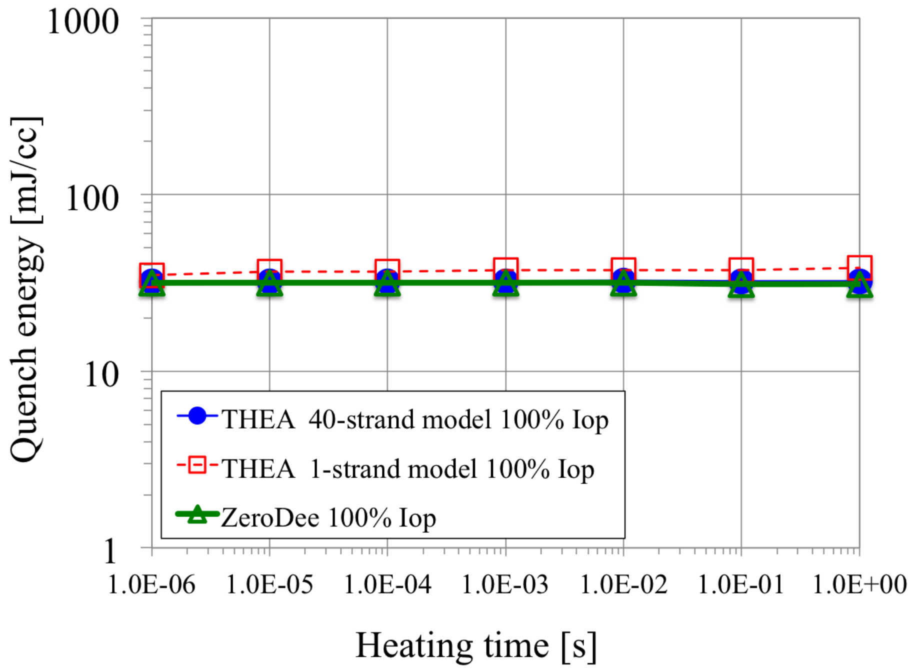

Figure 4.3 Comparison between the 0-D and 1-D models for high values of current.

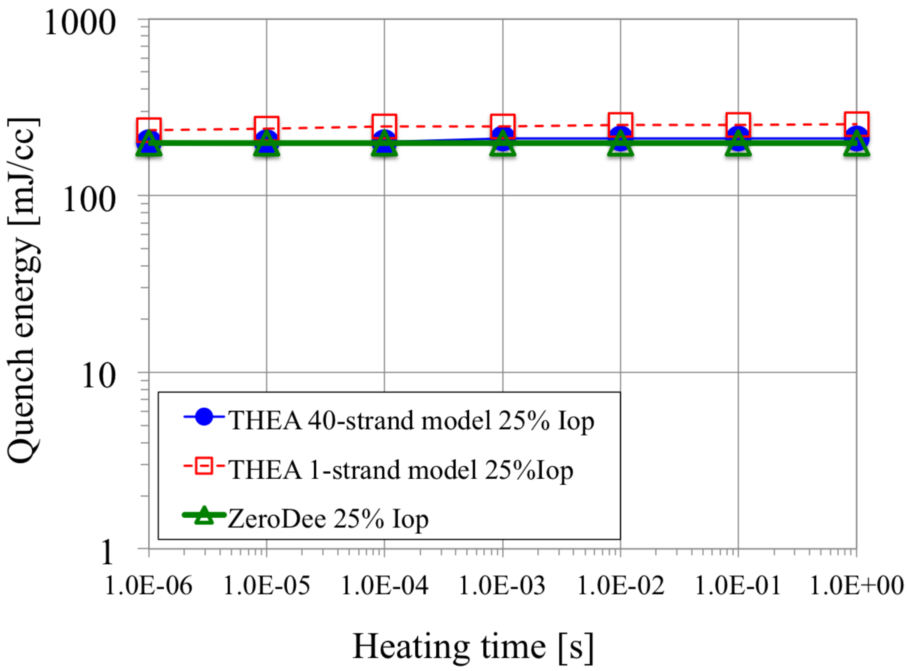

Figure 4.4 Comparison between the 0-D and 1-D models for low values of transport current.

amount of computation time, with respect to the more complex one-dimensional model.

5. The 1-D Approach

Increasing the level of complexity of the model, three different domains are analysed: thermal, electric and hydraulic elements are taken into account. Neglecting the cable cross section in comparison with the longitudinal dimension, a 1-D model can be considered. A schematic representation of the model conditions and parameters is shown in *Fig. 5.1*.

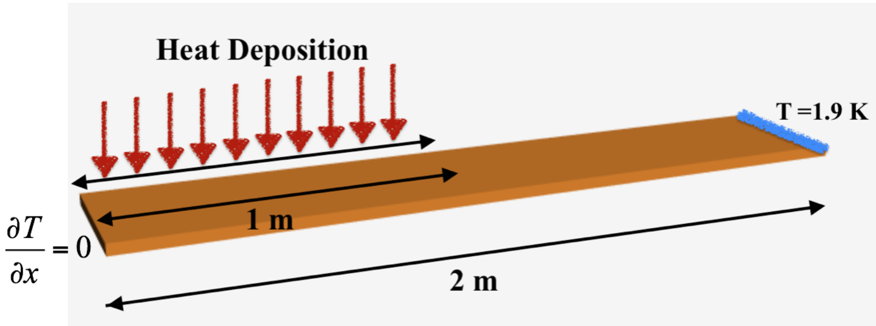

Figure 5.1 One-dimensional model overview

The analysed cable is four metres long, but, thanks to the symmetry condition on the left side, just half cable can be considered. So, with regard to the simulation, the length of the cable is $L_{cable} = 2\ m$. The heat disturbance starts at $t = 0$, with a duration Q_τ, affecting the first half of the cable, from $x = 0$ to $x = 1\ m$. The details of the heat deposition distribution, both in time and in space, will be discussed in section 5.5. The modelling and the simulations are carried out by means of the *THEA* [5] software. Acronym of Thermal Hydraulic Electric Analysis, this CryoSoft package allows to carry out one-dimensional analyses involving these three different domains. Basically, it allows to take into account not only the thermal phenomena of heat exchange, but also the current redistribution between strands and the fluid-dynamic behaviour of the liquid Helium. A detailed description of the three models is presented below.

5.1 Thermal model

The thermal model is described using N thermal elements: the number of the strands and the glass-epoxy. The strand is considered as a homogenous composite of Nb_3Sn and Cu with uniform temperature in the cross section. Neglecting the transverse dimension the thermal model can be described through the one dimensional heat equation *(5.1)* [6]:

$$A_i \rho_i C_i \frac{\partial T_i}{\partial t} - \frac{\partial T_i}{\partial x}(A_i k_i \frac{\partial T_i}{\partial x}) = \dot{q}'_{St} + \dot{q}'_{Joule} + \sum_{j=1, j\neq i}^{N} \frac{(T_j - T_i)}{H_{ij}} + \sum_{h=1}^{M} p_{ih} h_{ih} (T_h - T_i) \tag{5.1}$$

List of symbols used in the *(5.1)* equation		
A_i	$[m^2]$	cross section of the i-th component
ρ_i	$[Kg/m^3]$	density of the i-th component
C_i	$[J/KgK]$	specific heat of the i-th component
k_i	$[W/mK]$	thermal conductivity of the i-th component
T_i	$[K]$	temperature of the i-th component
$\dot{q}'_{St}$	$[W/m]$	external heat input per unit lenght
$\dot{q}'_{Joule}$	$[W/m]$	generated Joule power per unit leght
H_{ij}	$[Km/W]$	thermal resistance between i-th and j-th component
p_{ih}	$[m]$	wetted perimeter between the i-th and the h-th component
h_{ih}	$[W/m^2K]$	heat transfer coefficient between the i-th and the h-th component
N		number of thermal element $= N_{strand} + 1$
M		number of hydraulic element $= 1$

Table 5.1 List of symbols used in the *(5.1)* equation

The penultimate term of the right hand side of the *(5.1)* represent the heat exchange between thermal elements, while the last one indicate the heat exchange with the hydraulic elements.

As *Fig. 5.2* shows the heat exchange can occur between:

- adjacent and non-adjacent strands

- strands and glass-epoxy
- glass-epoxy and Helium bath (hydraulic element)

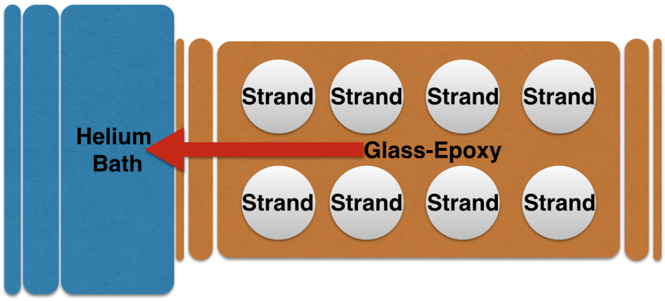

Figure 5.2 Thermal model representation

Is important to underline that there is NO contact between the strands and the Helium bath, and the heat exchange can occur only by means of the glass-epoxy.

5.1.1 Heat exchange between strands

The heat exchange between different strands is governed by the presence of thermal resistances H_{ij}. An accurate analysis and explanation of this phenomenon is presented in [7] *(in the section 2.5)*. For this analysis, the LCH 01 cable is considered, with the thermal conductance between adjacent strands $\lambda_{th-A} = 5000\frac{W}{Km^2}$ and the cross contact between non-adjacent strands $\lambda_{th-C} = 2500\frac{W}{Km^2}$ *. Starting from these conductances is possible to calculate the thermal resistances:

$$H_{ij} = \frac{l_{ij}}{\lambda_{ij} A_{ij}} \tag{5.2}$$

where l_{ij} is the length of the contact between the strands i-th and j-th, and A_{ij} is the total cross section contact between the strands i-th and j-th. As explained in [7] the contact area between strands can be calculated by a linear fit, for non-adjacent

*The real values of the contact thermal conductances for Nb_3Sn are still unknown, but in the next chapters it is demonstrated that the variation of these parameters should not affect the stability margin of the cable in a relevant way strands $A_c = 1.55 - 0.058x[mm^2]$ and for adjacent strands $A_a = 461 - 11.9x[mm^2/m]$, where x is the cable width position $[mm]$. Choosing a value of x equal to the cable width divided by two, the results shown in *Table 5.2* have been obtained.

A_a	$[mm^2/m]$	353.01
A_c	$[mm]$	1.024

Table 5.2 Contact area between strands in $x = w/2$

The total cross section contact A_{ij} between the i-th and the j-th strands assumes two different values for adjacent and non-adjacent strands.

$$A_{ij} = \begin{cases} A_a l_{ij} & \text{for adjacent strands} \\ 2A_c l_{ij}/L_p & \text{for non-adjacent strands} \end{cases}$$

It's important to note that non-adjacent strands overlap two times in a twist pitch L_p

5.1.2 Heat exchange between strand and glass-epoxy

The model of the heat exchange between the strands and the glass-epoxy is shown in *Fig. 5.3*.

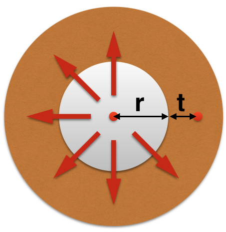

Figure 5.3 Heat exchange between strand and glass-epoxy representation

Each strand is surrounded by a crown of insulator, with an area equal to

$$A_{GE} = \frac{A_{GE-tot}}{40} = 4.98 \cdot 10^{-6} m^2$$

The total area of glass-epoxy is calculated through the difference between the whole area of the cable and the sum of each strand area

$$A_{GE-tot} = A_{Cable} - A_{St} = hw - 40\pi r^2$$

where h is the cable mid-thickness, w is the cable width and r is the radius of a strand.

The contact perimeter is the strand circumference and the thermal resistance is calculated as follow

$$H_{St-GE} = \frac{\frac{r}{K_{St}} + \frac{t}{K_{GE}}}{2\pi r}$$

where K_{St} and K_{GE} are the thermal conductivity of the strand and the glass-epoxy, and t is the half-thickness of the insulator crown. Is important to highlight that the contact thermal resistance between the strand and the glass-epoxy is unknown, and is not taken into account. †

5.1.3 The heat exchange between glass-epoxy and Helium bath

As the *Fig. 3.2* shows, the Helium bath is located in the internal zone of the quadrupole, therefore only the *thin face* of inner layer cables is in contact with the liquid Helium. The heat transfer coefficient (HTC) between the cable and the coolant is computed using empirical correlation. It is based on experimental data of [8], calculating the HTC from experimental curve of power extracted in steady state from the whole cable by the helium bath, through the *little face*: $Q_{estr}(T)$. This power is then normalised to the thin surface of the stack involved in the thermal exchange. The normalised power Q_{face} is used for the HTC_{HeBath}, expressed in $[W/m^2K]$.

$$HTC_{HeBath} = \frac{Q_{face}}{\Delta T A_{face}}$$

†In the next chapters it is demonstrated that the variation of the amount of glass-epoxy does not affect the stability margin of the cable in a relevant way. It is licit to suppose that the value of the thermal resistance between the strands and the insulator, should not be relevant as regard the stability of the system.

where ΔT is the difference between the stack wall and the He bath temperature, in $[K]$, and A_{face} is the surface of the stack involved in the heat exchange, expressed in $[m^2]$.

5.1.4 Thermal boundary and initial conditions

As far as the boundary conditions are concerned, a symmetry condition is imposed on the left side ($x = 0$):

$$\frac{\partial T}{\partial t} = 0$$

while on the right side ($x = L_{cable}$) the temperature is kept constant

$$T = 1.9\ K$$

Finally, before the introduction of the heat disturbance, at $t = 0$ the temperature is uniform and equal to $1.9K$ in the whole cable.

5.2 Hydraulic model

The hydraulic model is described by non-conservative form of the flow equation [6]:

$$\rho_h \frac{\partial V_h}{\partial t} + \frac{\rho_h V_h}{A_h}\frac{\partial V_h}{\partial x} + A_h \frac{\partial p_h}{\partial x} - \frac{\rho_h V_h^2}{A_h^2}\frac{\partial A_h}{\partial x} = -A_h F_h - \sum_{k=1,k\neq h}^{H} (\Gamma^{\nu}_{hk} - \nu \Gamma^{\rho}_{hk}) \tag{5.3a}$$

$$A_h \frac{\partial p_h}{\partial t} + V_h \frac{\partial p_h}{\partial x} + \rho_h + c_h^2 \frac{\partial V_h}{\partial x} =$$
$$\sum_{k=1,k\neq h}^{H} \left\{ c_h^2 \Gamma^{\rho}_{hk} + \varphi_h \left[\Gamma^{e}_{hk} \Gamma^{\nu}_{hk} - \left(h_h - \frac{\nu_h^2}{2} \right) \Gamma^{\rho}_{hk} \right] \right\} + \varphi_h V_h F_h + \varphi_h \dot{q}'_h + \varphi_h \dot{q}'_{cf,h} \tag{5.3b}$$

$$A_h \rho_h C_h \frac{\partial T_h}{\partial t} + A_h V_h C_h \frac{\partial T_h}{\partial x} + \rho_h \varphi_h C_h T_h \frac{\partial V_h}{\partial x} =$$
$$V_h F_h - \sum_{k=1,k\neq h}^{H} \left[\Gamma^{e}_{hk} \Gamma^{\nu}_{hk} - \left(h_h - \frac{\nu_h^2}{2} \right) - \rho_h C_h T_h) \Gamma^{\rho}_{hk} \right] + \dot{q}'_h + \dot{q}'_{cf,h} \tag{5.3c}$$

List of symbols used in the *(5.3)* equation		
A_h	$[m^2]$	cross section of the channel
ρ_h	$[Kg/m^3]$	density
C_h	$[J/KgK]$	specific heat at constant volume
c_h	$[m/s]$	isentropic sound speed
F_h	$[Kg/m^2s^2]$	friction force per unit of volume
φ_h		Gruneisen parameter
$\dot{q}'_h$	$[W/m]$	heat through convection
$\dot{q}'_{cf,h}$	$[W/m]$	heat through counterflow
h_h	$[J/Kg]$	specific enthalpy
p_h	$[Pa]$	pressure
T_h	$[K]$	temperature
V_h	$[m^3/s]$	volumetric flow
v_h	$[m/s]$	velocity of the coolant in the channel

Table 5.3 List of symbols used in the *(5.1)* equation

where the quantities Γ^{ρ}_{hk}, Γ^{ν}_{hk} and Γ^{e}_{hk} are the distributed sources of mass, momentum and stagnantion enthalpy per unit length of the channel, operating from (or into) h to (or from) the k channels. Geometrical parameters of the model are constant in time and space, and the friction factor model is based on Katheder model [25].

5.2.1 Hydraulic boundary and initial conditions

A closed pipe condition is set on the left side of the cable:

$$V_h = 0$$

while on the right side a reservoir condition has been chosen, imposing constant temperature and pressure:

$$T_h = 1.9\ K$$
$$p_h = 1.3\ bar$$

5.3 Electric model

The electrical model describes the cable as formed by E electrical elements characterised by longitudinal, mutual and self, inductances [6].In *Fig. 5.4* the connection between strands of the electric model is represented. The voltage balance equation along the cable can be written in matrix form as follows:

$$\mathbf{L}\frac{\partial \mathbf{T}}{\partial t} + \mathbf{RI} - \frac{\partial}{\partial x}(\mathbf{C}^{-1}\frac{\partial \mathbf{I}}{\partial x}) = \Delta \mathbf{V}^{ext} \tag{5.5}$$

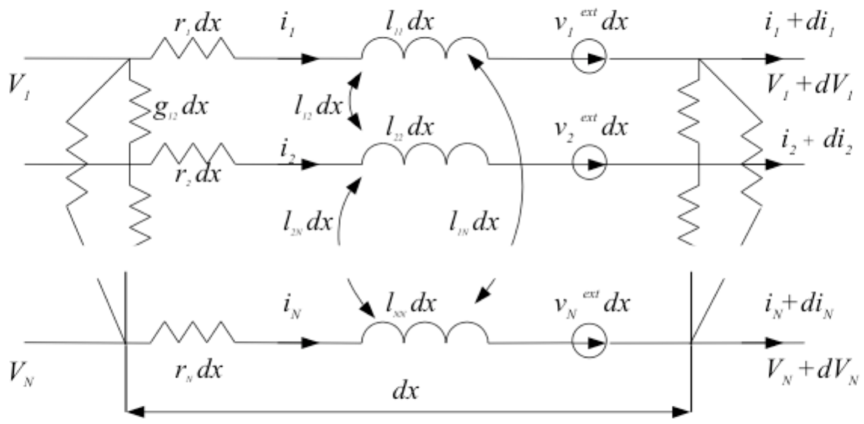

Figure 5.4 Electrical model representation

List of symbols used in the *(5.5)* equation	
$\mathbf{L}$	inductance per unit length matrix
$\mathbf{I}$	current array
$\mathbf{R}$	parallel resistances array
$\mathbf{C}$	transverse condictivities per unit length aray
$\Delta\mathbf{V}^{ext}$	external voltage array

Table 5.4 List of symbols used in the *(5.5)* equation

Each strand is considered as an electric element, where the current density in the cross section is assumed constant. The electric model is coupled with the thermal one, in order to take into account the dependance of the electric parameters on the temperature, the $\dot{q}'_{Joule}$ generated by the current flow and the current redistribution along the cable between different strands, depending both on the magnetic field and on the temperature profiles. Indeed the currents tend to redistribute towards regions of low field and temperature, and they try to avoid the zones where these two parameters take the maximal values.

5.3.1 Mutual and self-inductance

The inductance per unit length matrix is defined as follows:

$$\mathbf{L} = \begin{bmatrix} l_{ij} & \dots & l_{iN_{strand}} \\ \vdots & \ddots & \vdots \\ l_{N_{strand}j} & \dots & l_{N_{strand}N_{strand}} \end{bmatrix} \tag{5.6}$$

where l_{ij} is a mutual-inductance if $i \neq j$ or a self-inductance if $i = j$. The analysis of inductance of circuits made up of straight elements with negligible cross section is presented in [26]. Applying the general formula for the self-inductance of a round wire, and neglecting the ratio between the arithmetic mean distance of the points of the cross section and the cable length, the following formula is obtained:

$$l_{ij} = \frac{\mu_0}{2\pi}\left[ln\left(\frac{2L_i}{\rho_i} - \frac{3}{4}\right)\right] \quad \text{for } i = j \tag{5.7}$$

While the mutual-inductance between two parallel straight filaments is given by:

$$l_{ij} = \frac{\mu_0}{2\pi}\left[ln\left(\frac{L_i}{d_{ij}} + \sqrt{1 + \frac{L_i^2}{d_{ij}^2}}\right) - \sqrt{1 + \frac{L_i^2}{d_{ij}^2}} + \frac{d_{ij}}{L_i}\right] \quad \text{for } i \neq j \tag{5.8}$$

The distance between the $i - th$ and $j - th$ strands is calculated as follows:

$$d_{ij} = \sqrt{(x_i - x_j)^2 + (y_i - y_j)^2} \tag{5.9}$$

List of symbols used in the *(5.7)* and *(5.8)* equations			
ρ_i	$[m]$	$4.25 \cdot 10^{-4}$	strand radius
L_p	$[m]$	0.109	twist pitch
L_i	$[m]$	$3L_p$	filament length
d_{ij}	$[m]$	*eq.(5.9)*	distance between the strands
μ_0	$[H/m]$	$1.25663... \cdot 10^{-6}$	vacuum permeability

Table 5.5 List of symbols used in the *(5.7)* and *(5.8)* equations

The strands follow the numeration shows in *Fig. 5.5*, therefore the x and y coordinates values are given by:

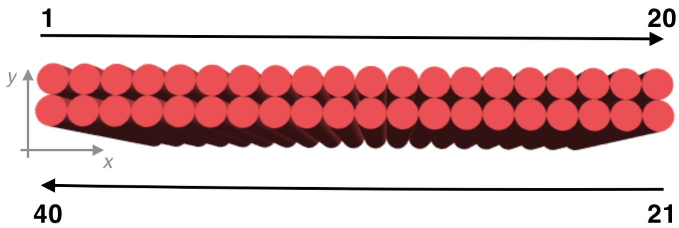

Figure 5.5 Representation of the strands numeration

$$x_i = 2\rho(i-1); \quad y_i = 2\rho \qquad \text{if } i \leq \frac{N_{strand}}{2}$$

$$x_i = 2\rho(N_{strand} - i); \quad y_i = 0 \qquad \text{if } i \geq \frac{N_{strand}}{2}$$

This is true only if the complete model of the Rutherford cable is considered. A numerical calculation of the inductance between two strands i and j of a volume V_i and V_j is fully treated in [27].

5.3.2 Conductance calculation

The conductance per unit length matrix is defined as follows:

$$\mathbf{C} = \begin{bmatrix} 0 & g_{ij} & \cdots & g_{iN_{strand}} \\ g_{ij} & \ddots & \ddots & \vdots \\ \vdots & \ddots & \ddots & g_{ij} \\ g_{N_{strand}j} & \cdots & g_{ij} & 0 \end{bmatrix} \tag{5.11}$$

Obviously, the conductance of a strand with itself is equal to zero. Depending on the strands position and taking into account the *Fig. 5.5*, the electric conductance can be:

$$g_{ij} = \begin{cases} g_c & \text{if } |i-j| = 1 \text{ or } |i-j| = N_{strand} - 1 \\ g_a & \text{if } |i-j| \geq 1 \end{cases}$$

where g_c is the conductance for non-adjacent strands and g_a is the conductance for adjacent strands , calculated as follows:

$$g_c = \frac{2}{L_p R_c}$$

$$g_a = \frac{2(N_{strand} - 1)}{L_p R_a}$$

The contact resistances for adjacent and non-adjacent strands, R_c and R_a, have been chosen with the same values of the $NbTi$ cables [9], in accord to [7]: $R_c = 40\mu\Omega$ and $R_a = 320\mu\Omega$. ‡

‡The real values of the contact resistances for Nb_3Sn are still unknown, but in the next chapters it is demonstrated that the variation of these parameters should not affect the stability margin of the cable in a relevant way

5.3.3 Electric boundary and initial conditions

Both in the left side ($x = 0$) and the right side ($x = L_{cable}$) all the strands are shorted together and the voltage differences are, by definition, equal to zero. At $t = 0$ the current is uniformly distributed in each strand with the value of I_{tot}/N_{strand}.

5.4 Magnetic field distribution

As *Fig. 5.6* shows, the magnetic field has a non-uniform distribution along the magnet. Each strand of inner-layer middle-plane cable is subjected to a variable field from 9.78 T to 2.42 T, following a linear behaviour shown in *Fig. 5.6*.

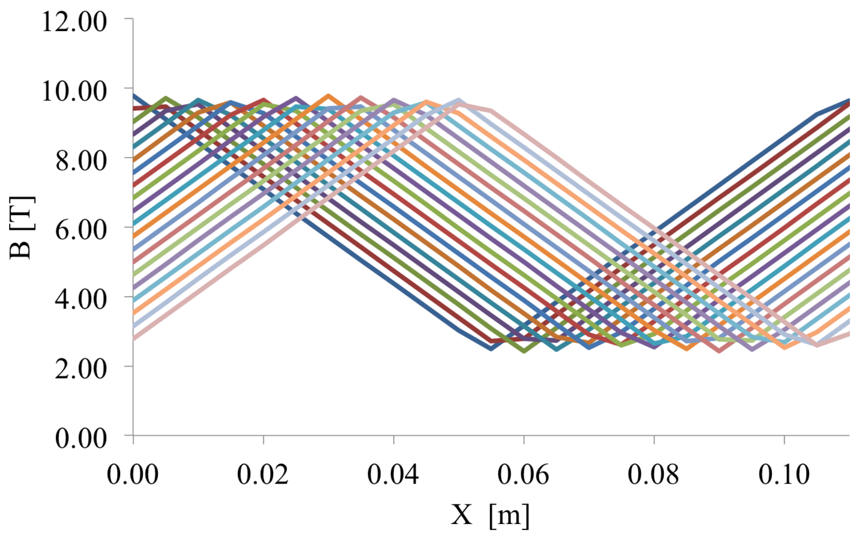

Figure 5.6 Linear magnetic field function along different strands

The profile of the field is the same for every strand, shifted on the space by a length of $s = L_P/N_{strand}$. It is important to underline, that the values of the magnetic field are depending on the current imposed in the cable, as *Table 5.6* shows [28].

The function chosen for the magnetic field profile of the $i-th$ strand is:

Values of magnetic field as a function of the operating current percentage $[I_{op} = 16.47kA]$		
I/I_{op}	$B_{max}[T]$	$B_{min}[T]$
100%	9.78	2.42
75%	7.48	1.85
50%	5.11	1.26
25%	2.63	0.65

Table 5.6 Values of magnetic field as a function of the operating current percentage

$$B_i(x) = \frac{B_{max} - Bmin}{\frac{L_p}{2}} \left[(x - c_{f,i} - \frac{L_p}{4}) - \frac{L_p}{2} \left\langle \frac{x - c_{f,i} - \frac{L_p}{4}}{\frac{L_p}{2}} + \frac{1}{2} \right\rangle \right] (-1)^{\left\langle \frac{x - c_{f,i} - \frac{L_p}{4}}{\frac{L_p}{2}} - \frac{1}{2} \right\rangle} + \frac{B_{max} + B_{min}}{2} \tag{5.12}$$

where the $\langle\rangle$ indicates the FLOOR function and $c_{f,i}$ is the shift coefficient, calculated as follows:

$$c_{f,i} = \frac{(i-1)L_p}{N_{strand}} \tag{5.13}$$

5.5 Heat disturbance

The heat deposition on the superconducting cable due to the beam losses is obtained by means of the *FLUKA* code [2]. It has been calculated that the value of the energy disturbance is maximum at the close vicinity of the bore and that decreases at larger distances. From the maps of heat deposition over the magnet cross-section, the longitudinal profile of the disturbance along each cable length has been computed. The curves have been approximated by an exponential low, characterised by consecutive increases and decays of the deposited energy *(5.14)*, as it is shown in *Fig. 5.7*.

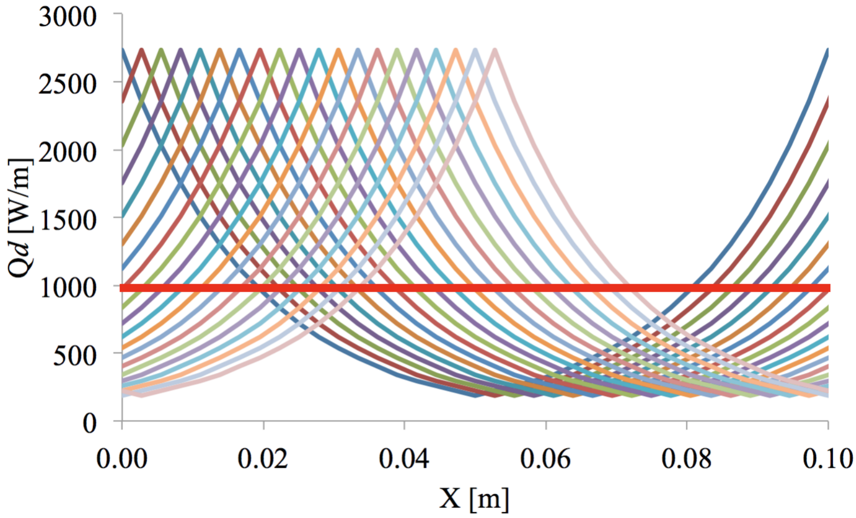

Figure 5.7 Profile of the heat deposition along different strands

$$Q_i(x) = Q_{ext,i} S_x S_t \frac{exp(E_c A(x - c_{f,i})}{exp(E_c A d L_p)} \quad (5.14)$$

$$A = (-1)^{\frac{2x}{L_p}}$$

$$d = \left\langle \frac{2x/L_p + 1}{2} \right\rangle$$

where $c_{f,i}$ is the shift coefficient already presented in *(5.13)*, E_c in a coefficient depending on the cable position (for middle-plane cables $E_c = -53.3$) [29], the $\langle\rangle$ indicate the FLOOR function, Q_{ext} is the peak value of the heat disturbance introduced by the user and the functions S_x and S_t are smoothing coefficient in space *(5.15)* and time *(5.16)*. The energy disturbance profile does not start or end sharply, and it is worth to explain the smoothing of the heat deposition function, both in the space and in the time. Considering a fall distance $\Delta x = (Q_{Xend} - Q_{Xbegin})/200$, where Q_{Xend} and Q_{Xbegin} are the extremities of the heated zone, the smoothing start at $x_1 = Q_{Xbegin} + \Delta x/2$ $x_2 = Q_{Xend} + \Delta x/2$:

$$S_x = \begin{cases} 1 & \text{if } x \leq x_1 \\ 1 - \frac{x-x_1}{x_2-x_2} & \text{if } x_1 < x \leq x_2 \end{cases} \tag{5.15}$$

On the left side there is no smoothing, due to the symmetry condition. Heating always starts at $t = 0$ and increase its value from $0 \quad W/m$ to Q_{ext} in $\Delta t = Q_\tau/10$, where Q_τ is the heating time set by the user. When the time becomes greater then $Q_\tau - \Delta t/2$ the function starts to decrease until $Q_\tau + \Delta t/2$, when it is set equal to $0 \quad W/m$ again.

$$S_t = \begin{cases} \frac{t}{\Delta t} & \text{if } 0 < t \leq \Delta t \\ 1 & \text{if } \Delta t < t \leq Q_\tau - \Delta t/2 \\ 1 - \frac{t-(Q_\tau - \Delta t/2)}{(Q_\tau + \Delta t/2)-(Q_\tau - \Delta t/2)} & \text{if } Q_\tau - \Delta t/2 < t \leq Q_\tau + \Delta t/2 \end{cases} \tag{5.16}$$

The horizontal red line in *(5.14)* represents the integral mean value of the function and it is useful to understand the quantity of energy introduced in the system.

5.6 Temperature and Current distributions

The use of the CryoSoft code THEA [5] allows to analyse with accuracy the distribution of temperature and current for each strand in both time and space. This feature permits a precise investigation of these parameters along the cable and a better comprehension of the behaviour of the strands in a specific configuration of magnetic field and heat deposition. In this section the phenomena that occur during a quench in the first strand of the $NbTi$ and Nb_3Sn cables have been analysed, in terms of temperature and current, in function of the strand length, at different instants of time. The same power disturbance has been induced in both cables for a duration of 10 μs. In *Fig. 5.8* and *Fig. 5.9* the temperature profiles are shown in comparison with the heat disturbance. For sufficiently short times, the temperature follows the trend of the energy disturbance: greater is the introduced heat, greater is the temperature increase.

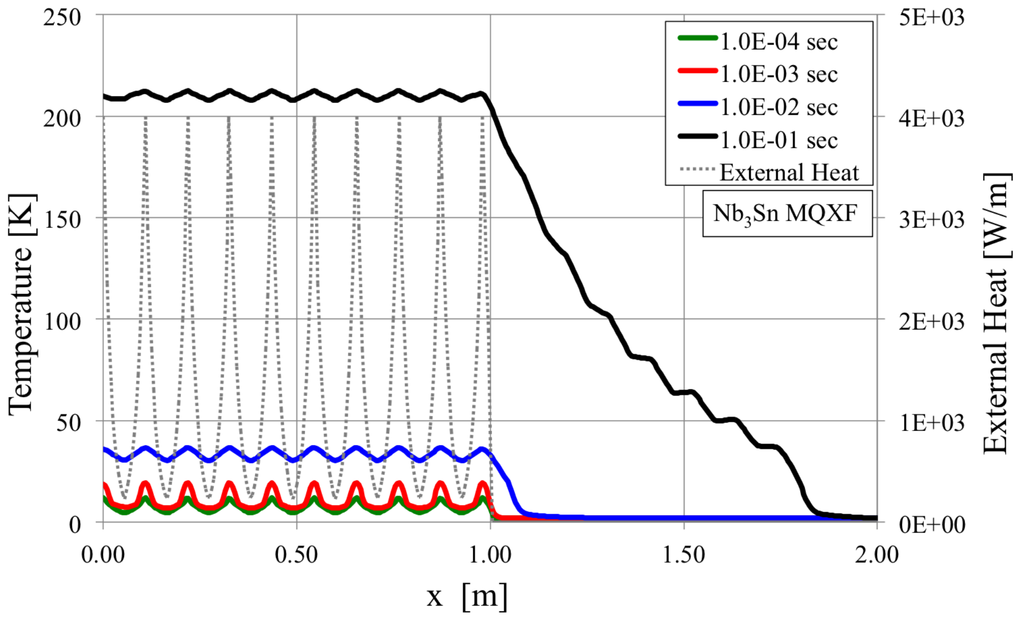

Figure 5.8 Profile of the temperature vs the heat disturbance of the first strands of a Nb_3Sn MQXF cable during the quench, induced by a heat disturbance of 10 μs.

However, although the imposed heat disturbance is almost the same, the two cables exhibit strong differences in the temperature strand distribution. After one second the Nb_3Sn reaches a very high value of temperature (over 200 K), while the $NbTi$ maintain its temperature below the 70 K. It is important to notice that the $NbTi$ shows a faster and more homogeneous normal zone propagation in comparison with the Nb_3Sn. In *Fig. 5.10* and *Fig. 5.11* the temperature profiles and the magnetic field are presented.

Furthermore, an inversion of the maximum and minimum trend can be observed in *Fig. 5.9* at times greater than 10 ms. As expected, at the beginning, the cable temperature follows the heat disturbance: a local maximum of the disturbance implies a local maximum of the temperature. While for the Nb_3Sn this relation remains true for the long times, for the $NbTi$ the electrical phenomena became predominant and the above-mentioned inversion occurs. As shown in *Fig. 5.11* after 10 ms, the temperature profile is in opposition with the magnetic field one. This

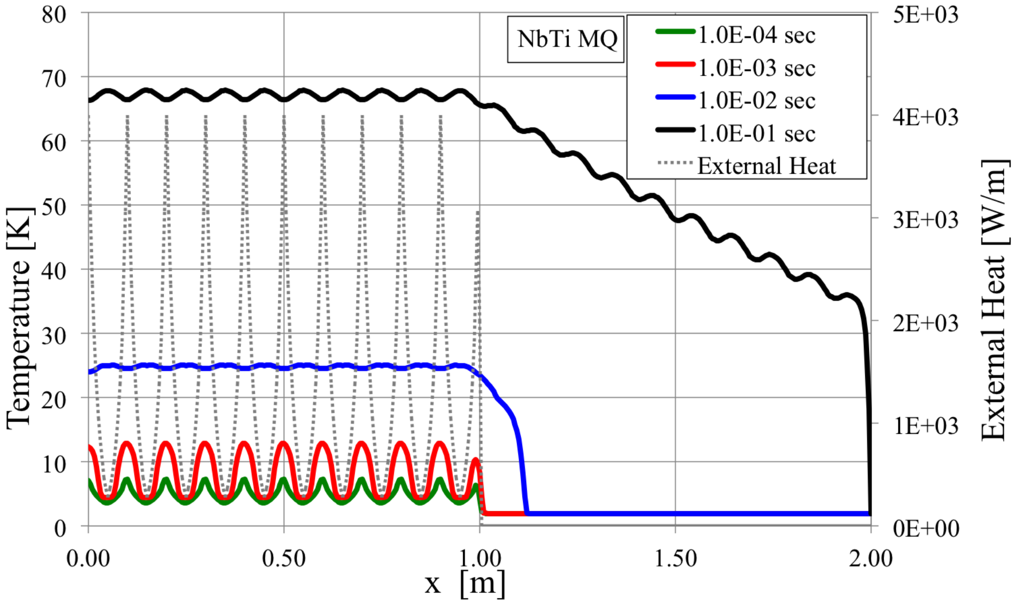

Figure 5.9 Profile of the temperature vs the heat disturbance of the first strands of a $NbTi$ MQ cable during the quench, induced by a heat disturbance of 10 μs.

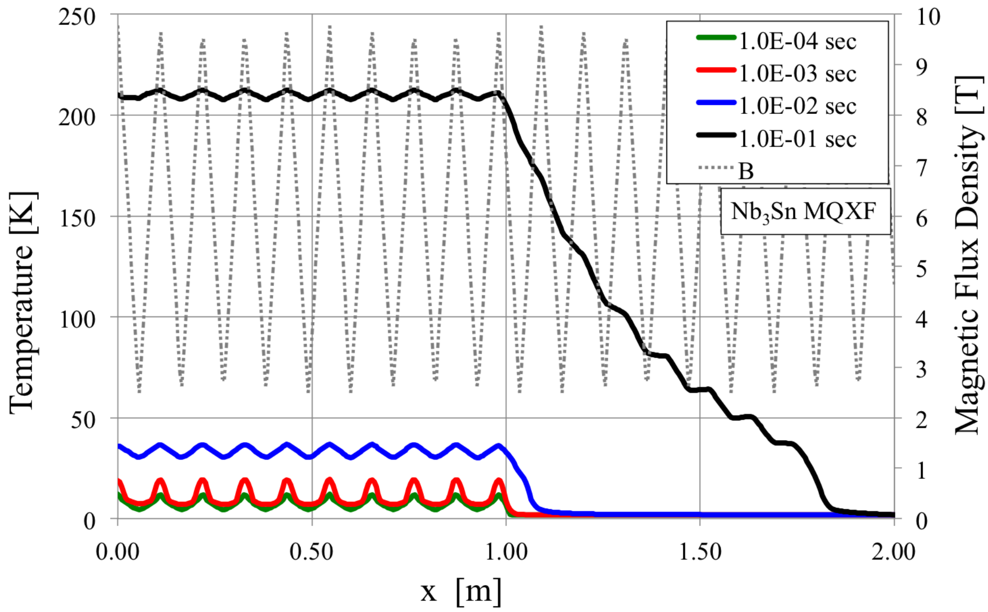

Figure 5.10 Profile of the temperature vs the applied magnetic field of the first strands of a Nb_3Sn MQXF cable during the quench, induced by a heat disturbance of 10 μs.

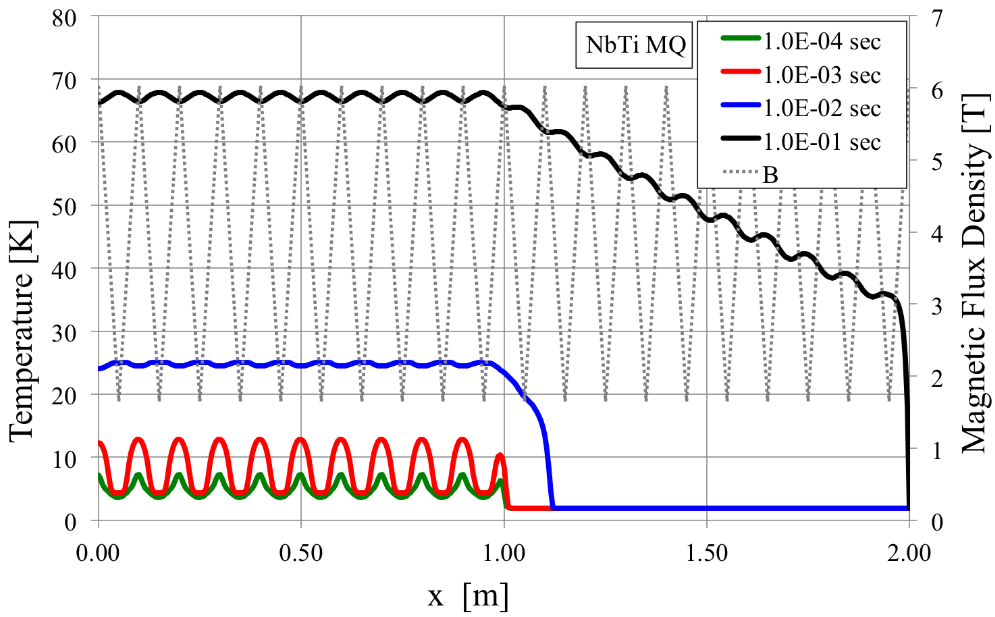

Figure 5.11 Profile of the temperature vs the applied magnetic field of the first strands of a *NbTi* MQ cable during the quench, induced by a heat disturbance of 10 μs.

phenomenon can be explained as follows: high values of magnetic field determines low value of current as shown in *Fig. 5.15*, that implies low value of Joule heating and consequently a lower increase of temperature. In this sense, for the *NbTi*, the electrical phenomena are predominant at long times.

The distribution of currents for Nb_3Sn and *NbTi* are shown, in comparison with heat disturbance and magnetic field, in *Fig. 5.12 Fig. 5.13* and *Fig. 5.14 Fig. 5.15* respectively.

Minimal values of both heat deposition and applied magnetic field imply maximal values of current. Of course the current tries to "escape" from high magnetic field and temperature, where the developed longitudinal electric field is higher. It is worth to notice the strong difference between the current oscillation values of the Nb_3Sn and *NbTi*. For the first cable the current variations of current are in the order of 5 %, while in the second one the amplitude of the oscillation is about 50 % of the nominal value. This means that the *NbTi* strand, contrary to the Nb_3Sn, can exchange a large quantity of current with the neighbouring strands. Comparing the temperature and current graphs, one can observe the advancing of the quench front by means of temperature increase and unstable current redistribution.

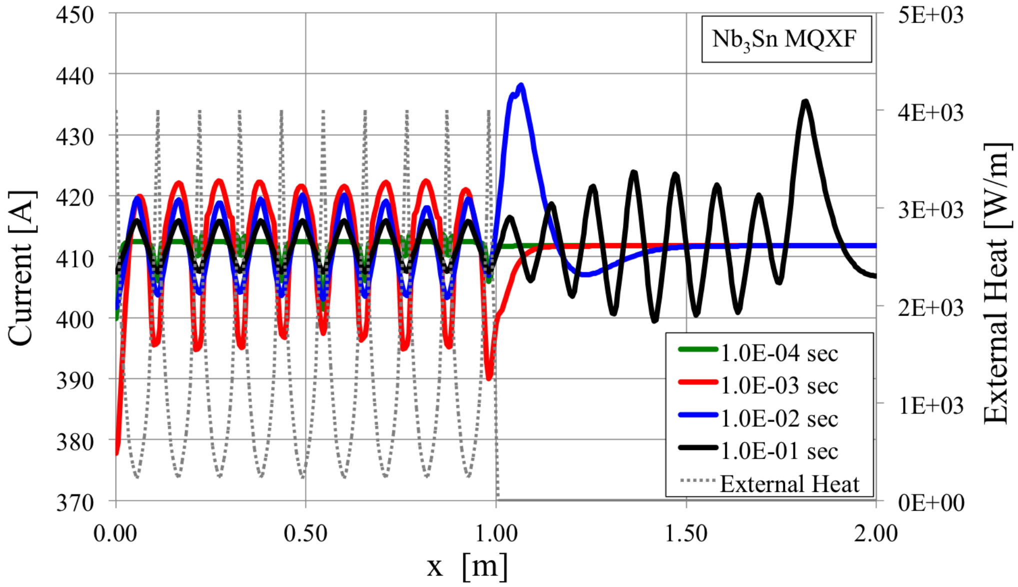

Figure 5.12 Profile of the current vs the heat disturbance field of the first strands of a Nb_3Sn MQXF cable during the quench, induced by a heat disturbance of 10 μs.

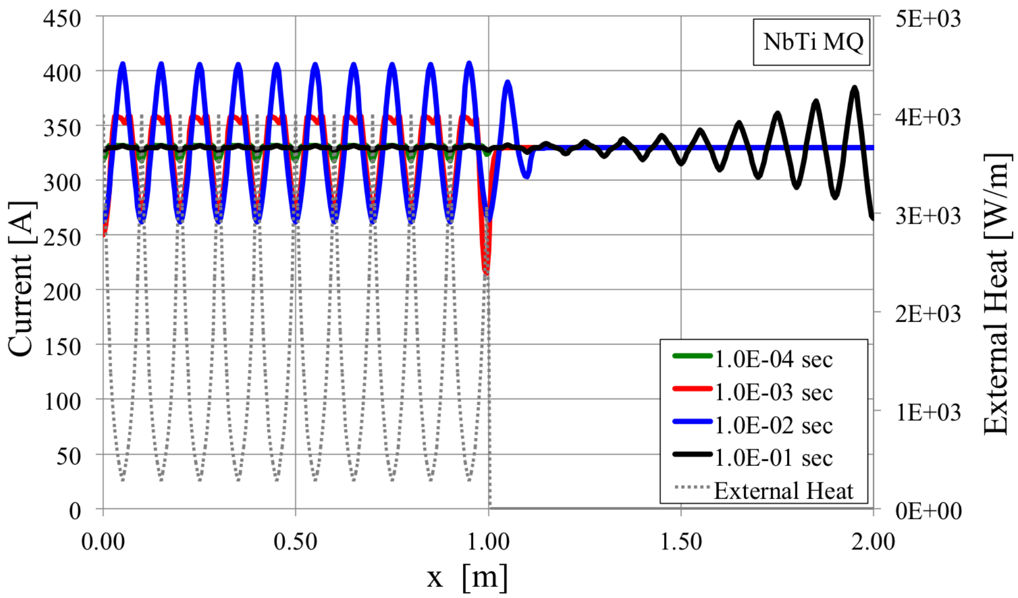

Figure 5.13 Profile of the current vs the heat disturbance field of the first strands of a $NbTi$ MQ cable during the quench, induced by a heat disturbance of 10 μs.

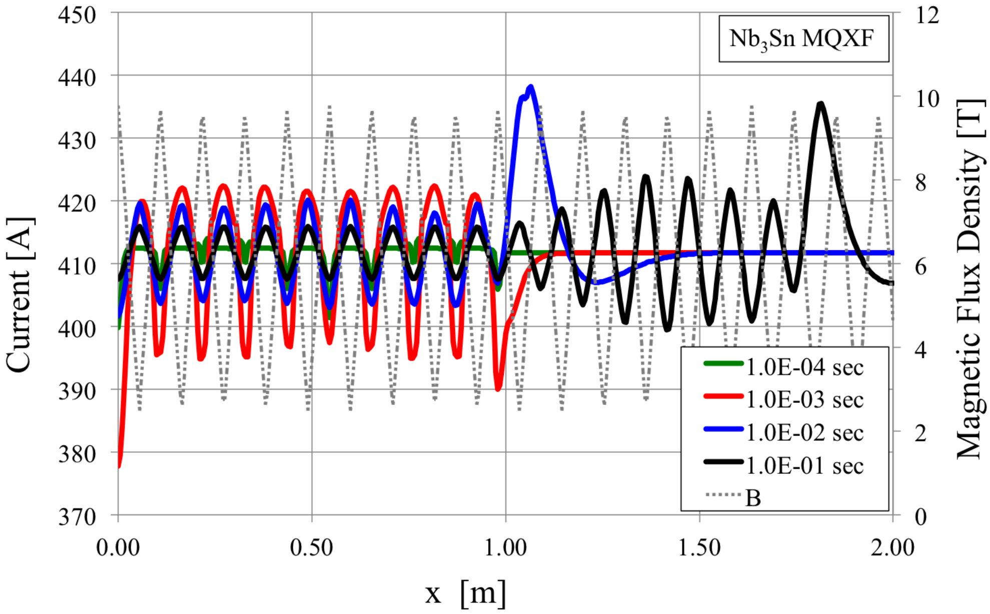

Figure 5.14 Profile of the current vs the applied magnetic field of the first strands of a Nb_3Sn MQXF cable during the quench, induced by a heat disturbance of 10 μs.

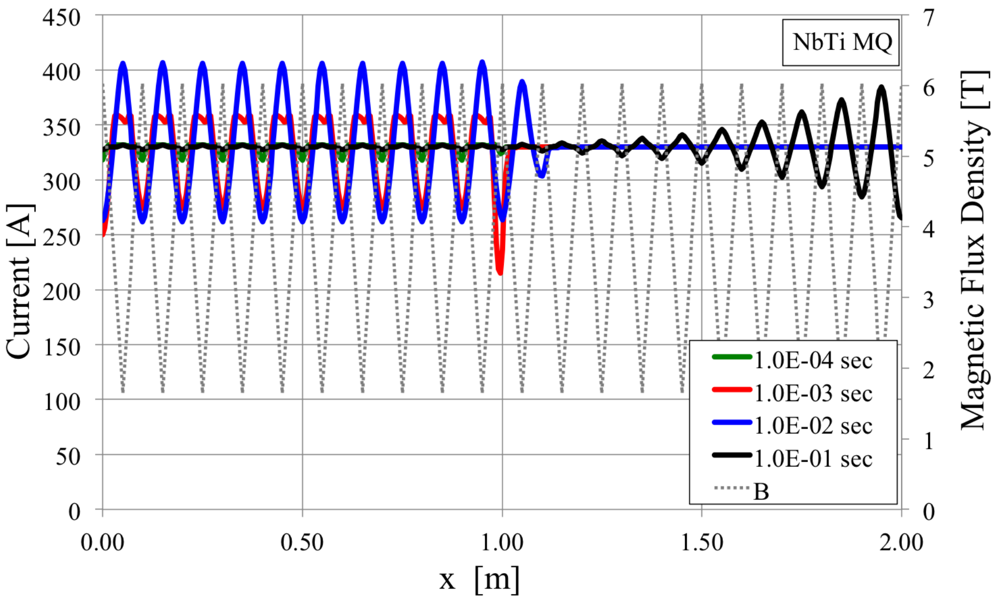

Figure 5.15 Profile of the current vs the applied magnetic field of the first strands of a $NbTi$ MQ cable during the quench, induced by a heat disturbance of 10 μs.

To sum up, Nb_3Sn and $NbTi$ exhibit strong differences both in terms of temperature and current distributions during quench. As it will be explained in the next paragraphs, the Nb_3Sn is characterised by a robust local behaviour, especially for fast time scale. That does not allow to exchange heat and current through neighbouring strands in efficient way, hence a stability improvement between the one-strand and the multi-strand model cannot be observed.

6. The 1-D model results

The results for the Nb_3Sn QXF cable 1-D dimensional model are presented in this chapter, both for the *1-strand* and the *40-strand* models. These two models give very similar result, as *Fig. 6.1* and *Fig. 6.3* show. This is a very important point and it will be deeply analysed. The quench energies are almost constant in the uniform case, while a quite significant increase can be observed at high values of heating time for the non-uniform heat deposition, especially at high currents. Another fundamental characteristic of the Nb_3Sn cables is the strong variation of their stability depending on the heating deposition mode. As *Fig. 6.2* and *Fig. 6.4* show, an uniform heat deposition implies a greater stability of the cable in comparison with the non-uniform MEAN case at low value of heating time. This is probably because, for fast time scale, the cable presents a local behaviour and each strands *"feels"* the maximum values of the heating power instead of the global mean value. On the other hand the non-uniform PEAK case gives higher energies than the uniform one, and it probably means that a certain quantity of energy can be redistributed along each strand length in more efficient way in the non-uniform heating. The *Fig. 6.3* exhibits that the stability margin of the Nb_3Sn at 100% of the operating current and with uniform heat deposition is almost coincident with the value of the cable enthalpy calculated from T_{op} and T_{cs}.

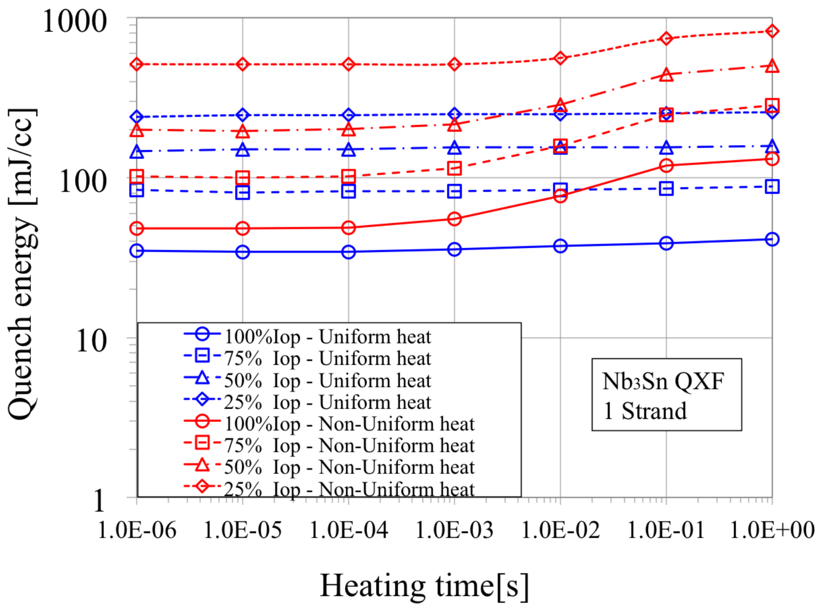

Figure 6.1 QXF Nb_3Sn: Quench energies vs. Heating time at different percentages of operating current $I_{op} = \frac{16.47}{40}\ kA$, for the *1-strand* model.

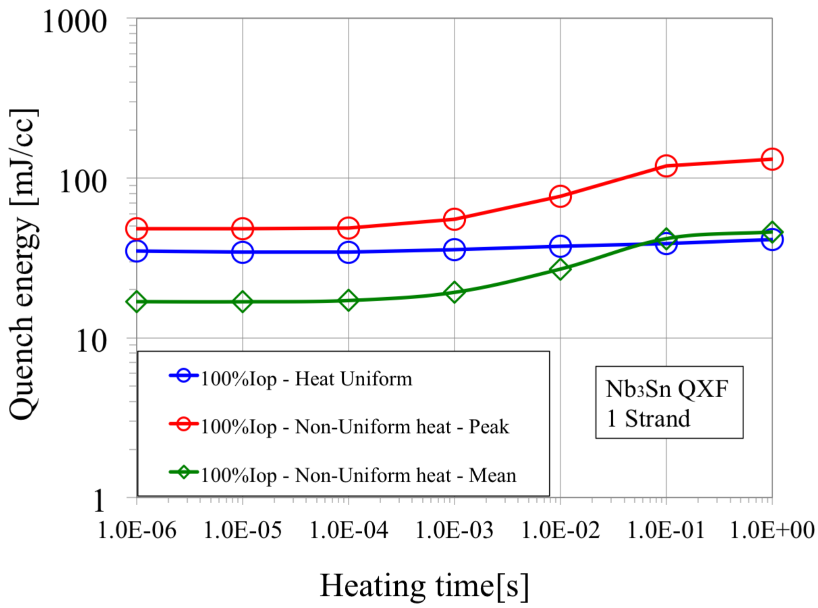

Figure 6.2 QXF Nb_3Sn: Quench energies vs. Heating time at the operating current $I_{op} = \frac{16.47}{40}\ kA$, for the *1-strand* model with uniform (blue curve), non-uniform PEAK (red curve) and non-uniform MEAN (green curve) heat deposition.

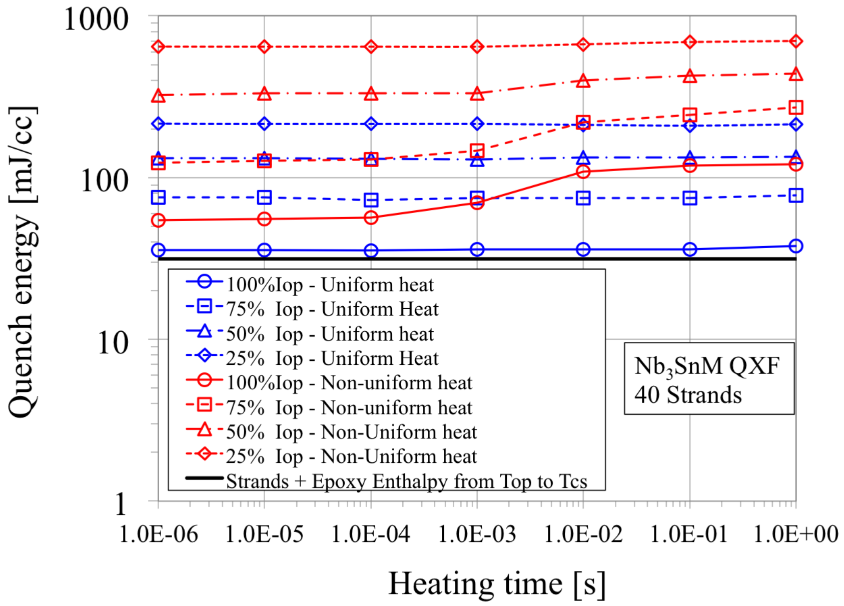

Figure 6.3 QXF Nb_3Sn: Quench energies vs. Heating time at different percentages of operating current $I_{op} = 16.47\ kA$, for the *40-strand* model with uniform (blue curves) and non-uniform PEAK (red curves) heat deposition.

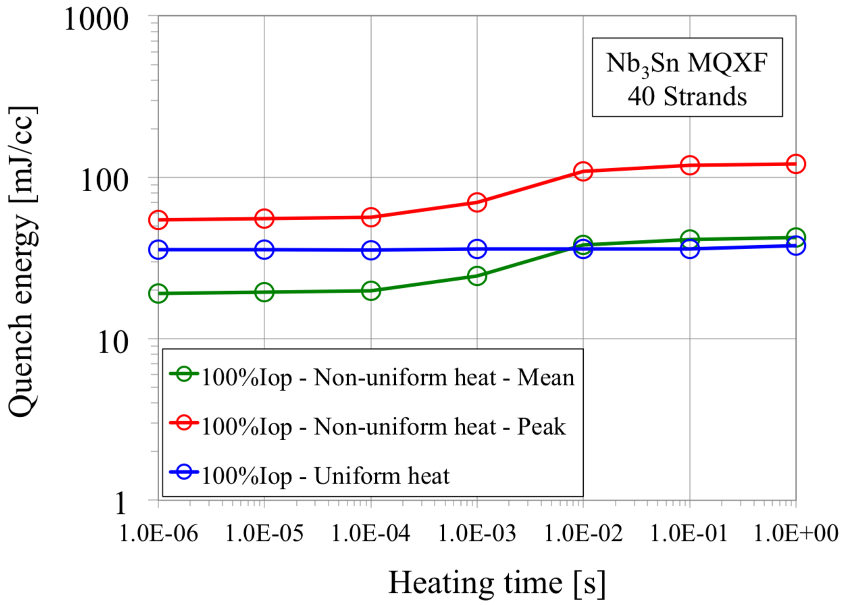

Figure 6.4 QXF Nb_3Sn: Quench energies vs. Heating time at the operating current $I_{op} = 16.47\ kA$, for the *40-strand* model with uniform (blue curve), non-uniform PEAK (red curve) and non-uniform MEAN (green curve) heat deposition.

6.1 Nb_3Sn and $NbTi$ cables comparison

The comparison between the Hi-Lumi LHC QXF Nb_3Sn and the LHC MQ $NbTi$ cables is presented in this section. The data and the results for the LHC $NbTi$ cables are taken from [9] and [30]. It is important to underline that, while in the QXF Nb_3Sn cable there is no contact between the strands and the helium bath, in the MQ $NbTi$ one, not only the strands are in direct contact with the helium bath, but they are also surrounded by the so-called *interstitial helium*. Therefore, it is obvious that for high values of heating time, where the heat exchange with the helium becomes predominant, the typical quench energies increase of the $NbTi$ cannot be observed in the Nb_3Sn cable. In *Table 6.1* the main data and operating parameters of both cables are shown. While the current density ratios are almost the same, the Nb_3Sn has a double temperature margin with respect to the $NbTi$. In fact, for the $1-strand$ analysis *Fig. 6.5*, an increase of 70% of quench energies can be observed in the Nb_3Sn in comparison with the $NbTi$ cable at fast heating time. However, when the complete model is taken into account, with 40 strands for the Nb_3Sn and with 36 strands for the $NbTi$, this gap is closed and both cables exhibit the same quench energies for low values of heating time *Fig. 6.6*. It is quite surprising that, despite the more demanding operating conditions, the simulations for the MQXF Nb_3Sn cables give comparable quench energies with the actual LHC MQ $NbTi$ cables, at least for low energy pulse duration.

The obvious question is: *"Why does the Nb_3Sn cable lose its advantage in the N-strand model?"*. Unfortunately the answer is not so obvious! As shown in *Fig. 6.7*, the $NbTi$ exhibits an increase of Quench Energies about 200% from the *1-strand* to the *36-strand* model. This means that the presence of other strands allows a good sharing of heat and current, increasing the stability of the cable.

A very different behaviour can be observed in the Nb_3Sn, (see *Fig. 6.8*), where the difference between the two models results barely 10%. The Nb_3Sn exhibits a local behaviour and the communication between different strands seems to be, somehow, inhibited.

	$\mathbf{Nb_3Sn}$	**NbTi**
Cable data		
Strand diameter [mm]	0.850	0.825
Number of strands	40	36
Cu/nonCu	**1.20**	**1.95**
Transposition pitch [mm]	109	100
Width [mm]	18.15	15.1
Operating conditions		
Total current [kA]	16.47	11.87
Current density [kA/mm^2]	1.6	1.8
Peak magnetic field [T]	11.4	6.85
Temperature [K]	1.9	1.9
$\mathbf{T_{cs} - T_{op}[K]}$	**5.34**	**2.89**
$T_c - T_{op}[K]$	10.94	5.04
$\mathbf{J_{op}/J_c}$	**0.472**	**0.465**

Table 6.1 Comparison between HiLumi LHC QXF Nb_3Sn and LHC MQ $NbTi$ cables

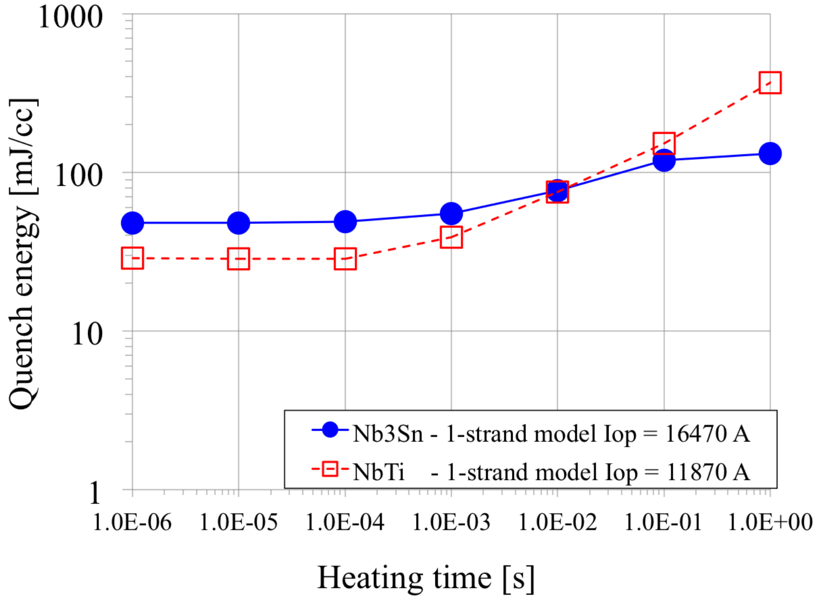

Figure 6.5 Comparison between QXF Nb_3Sn and MQ $NbTi$ cables: Quench energies vs. Heating time at the operating current, for the *1-strand* model with non-uniform heat deposition.

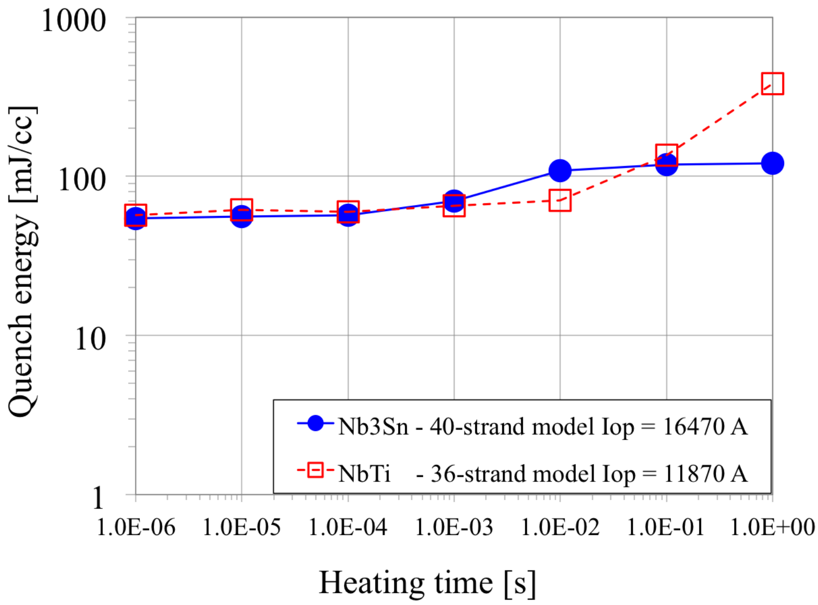

Figure 6.6 Comparison between QXF Nb_3Sn and MQ $NbTi$ cables: Quench energies vs. Heating time at the operating current, for the *N-strand* model with non-uniform heat deposition

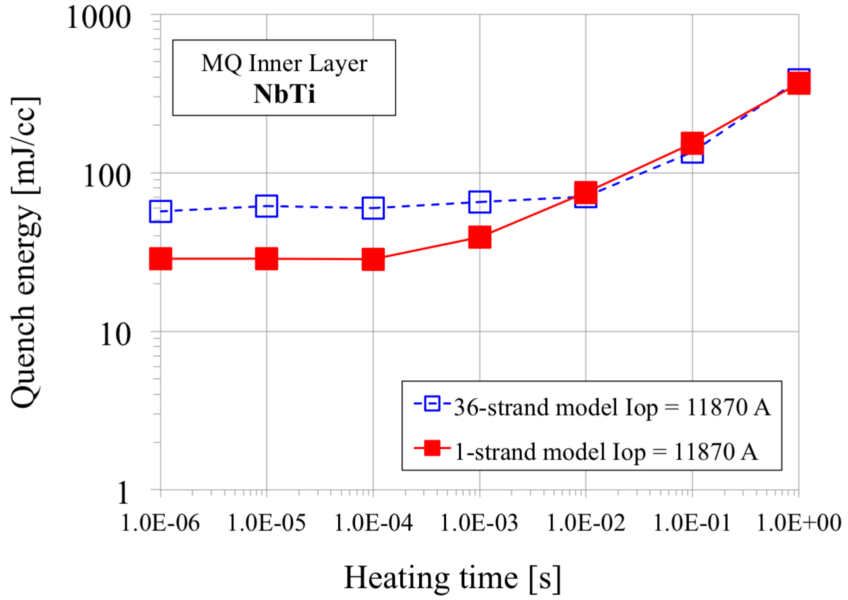

Figure 6.7 Comparison between *1-strand* and *36-strand* models for MQ $NbTi$ cable: Quench energies vs. Heating time at the operating current, with non-uniform heat deposition.

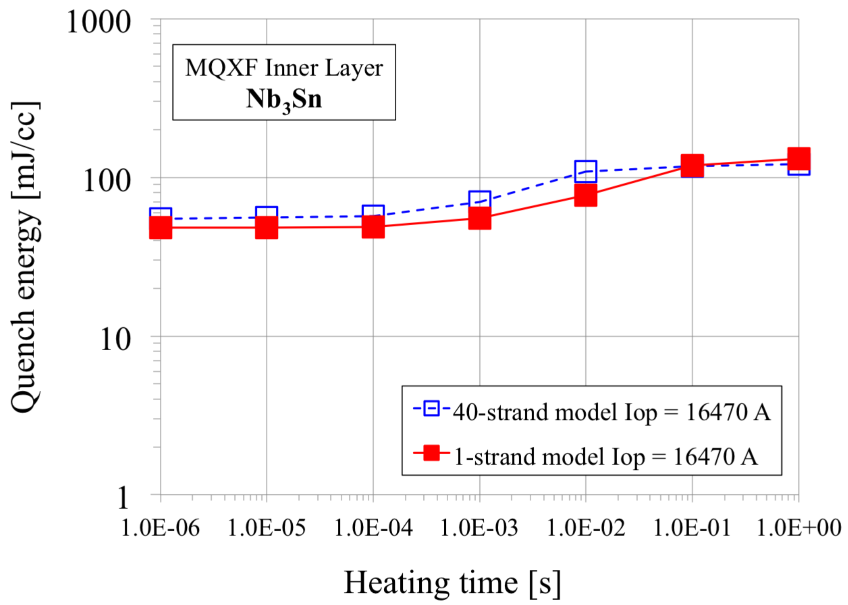

Figure 6.8 Comparison between *1-strand* and *40-strand* models for MQXF Nb_3Sn cable: Quench energies vs. Heating time at the operating current, with non-uniform heat deposition.

6.1.1 Stabiliser analysis - Copper

The thermal conductivity of the copper is much greater than the one of the superconductors, hence the main part of the heat is supposed to flow in the stabiliser. For this reason the amount of copper should play an important role in the stability of the cable and the $NbTi$ high value of the Cu/nonCu ratio could be responsible for the strong increase of quench energies observed in *Fig. 6.7.* In order to clarify this point, a new design of Nb_3Sn, with a Cu/nonCu equal to 1.95, has been simulated and the results are presented in *Fig. 6.9.*

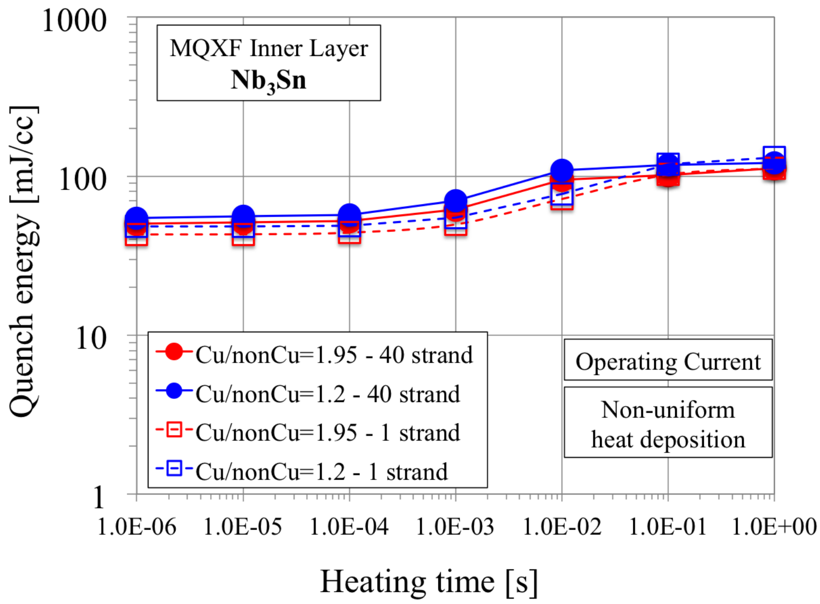

Figure 6.9 Comparison between different amounts of copper for the *1-strand* and the *40-strand* models for MQXF Nb_3Sn cable: Quench energies vs. Heating time at the operating current, with non-uniform heat deposition.

Very slight variations can be observed between the different cases, hence the amount of copper cannot be the explanation of the different behaviour of the cable from the $1-strand$ to the $N-strand$ model.

6.1.2 Thermal conductivity analysis

The Nb_3Sn has a thermal conductivity one or two orders of magnitude, depending on the temperature, lower than the $NbTi$ one. With the aim to understand the reason why these two materials present so different behaviours, the thermal conductivity of the Nb_3Sn has been virtually increased by a factor 50.

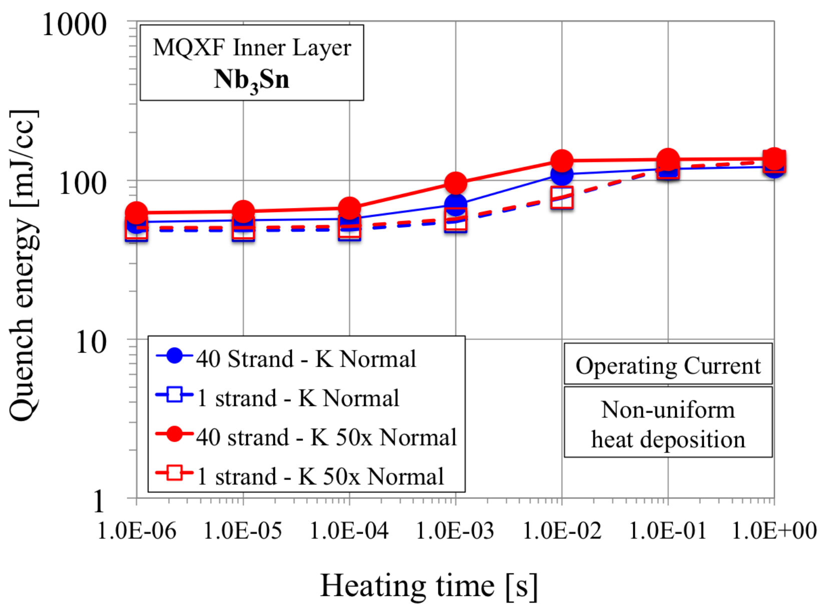

Figure 6.10 Comparison between different values of thermal conductivity for the *1-strand* and the *40-strand* models for MQXF Nb_3Sn cable: Quench energies vs. Heating time at the operating current, with non-uniform heat deposition.

As it is shown in *Fig. 6.10* no significant variations can be observed in the results, and the reason why a strong increase of the quench energies in the $N-strand$ model cannot be observed in the Nb_3Sn is still unknown.

6.1.3 Distribution of the heat deposition

Another key difference between Nb_3Sn and $NbTi$ is the response to the uniformity or non-uniformity of the heat deposition. In fact, if the $NbTi$ seems to be not affected by the heating mode *Fig. 6.11*, the Nb_3Sn exhibits an increase of quench energies greater than 80% if the heat is introduced into the system in the uniform way *Fig. 6.4*. Also this kind of analysis highlights the local behaviour of the Nb_3Sn strand, that perceives the peaks of the introduced energy, rather than the mean value as the $NbTi$.

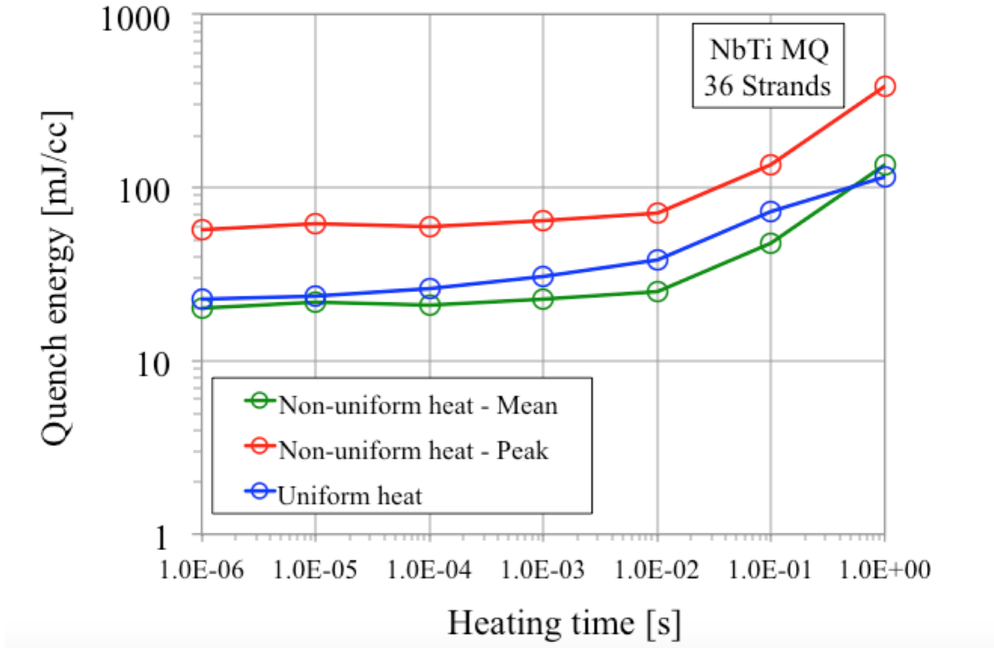

Figure 6.11 MQ $NbTi$: Quench energies vs. Heating time at the operating current , for the *36-strand* model with uniform (blue curve), non-uniform PEAK (red curve) and non-uniform MEAN (green curve) heat deposition.

6.1.4 Insulator analysis - Glass-epoxy

As it was specified several times above, the most relevant difference of the Nb_3Sn in respect with the $NbTi$ cables is the absence of the interstitial helium and the null wet perimeter between the strands and the helium bath. For a better comprehension of the importance of these working conditions, the interstitial helium has been removed from the $NbTi$ cable and glass epoxy has been inserted instead, excluding any possible contact between the strands and the helium bath. The *Fig. 6.12* and the *Fig. 6.13* show that, as expected, the absence of interstitial helium remarkably reduces the quench energies of the $NbTi$ cable, by a factor four in the $1-strand$ case and by a factor two in the $36-strand$ case. It is worth to note that the presence of glass-epoxy determines the same trend both for Nb_3Sn and $NbTi$.

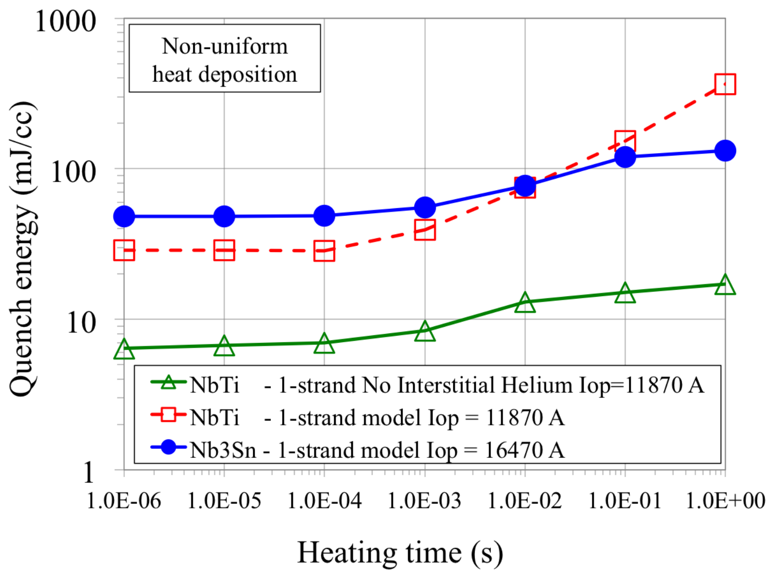

Figure 6.12 Comparison between the presence and the absence of interstitial helium, replaced with glass-epoxy, for the *1-strand* model for MQ $NbTi$ cable: Quench energies vs. Heating time at the operating current, with non-uniform heat deposition.

In order to investigate the role and the weight of the insulator in the QXF Nb_3Sn cable, a new one, characterised by one tenth of the *"correct"* glass-epoxy area, has been designed and simulated. The *Fig. 6.14* shows that no relevant variation can be observed in the quench energies, hence the insulator contribution to the thermal stability of the cable is basically negligible.

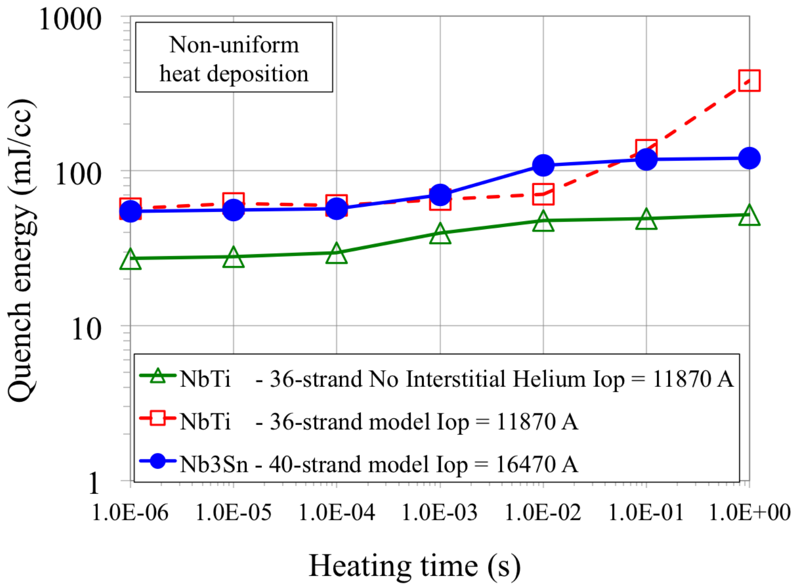

Figure 6.13 Comparison between the presence and the absence of interstitial helium, replaced with glass-epoxy, for the *36-strand* model for MQ $NbTi$ cable: Quench energies vs. Heating time at the operating current, with non-uniform heat deposition.

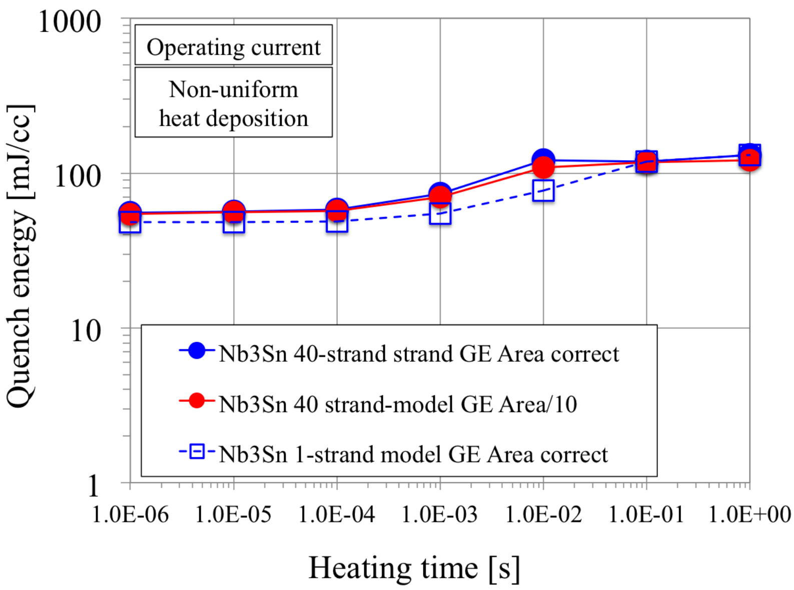

Figure 6.14 Comparison between different values of glass-epoxy area for the *40-strand* model for QXF Nb_3Sn cable: Quench energies vs. Heating time at the operating current, with non-uniform heat deposition.

6.2 Nb_3Sn cored cable

Increasing the level of complexity of the model, a stainless steel core $25\mu m$ thick and $12mm$ wide has been introduced as a new thermal element [1]. Due to the very high electric resistance of the core, the current is assumed not to flow in the longitudinal direction, therefore the core is not implemented as an electric element. According to [7] (*section 4.1.2*), the presence of the core induces a relevant increase of thermal and electrical resistances between non-adjacent strands: $\lambda_{th-C} = 500\ \frac{W}{Km^2}$ and $R_c = 10000\ \mu\Omega$. It is important to note that non-adjacent strands can exchange heat only through the core and the insulator, as it is shown in *Fig. 6.15*. The adjacent strands heat exchange is not affected by the presence of the core.

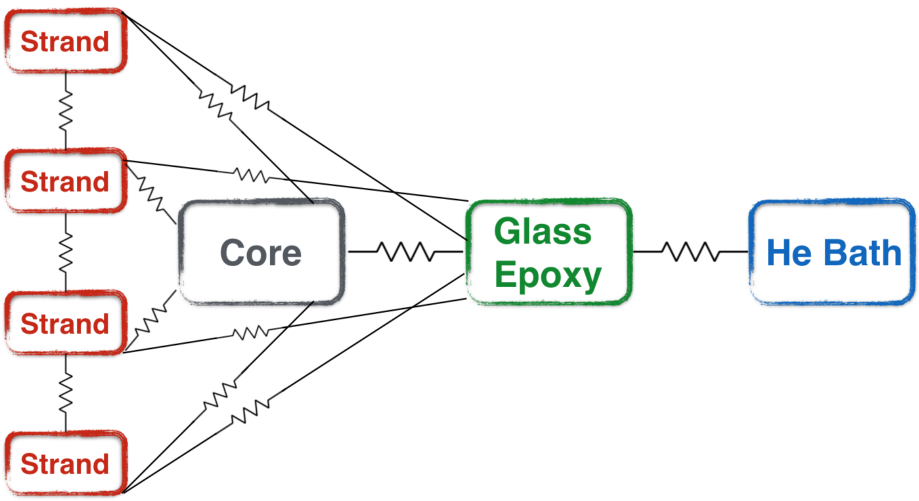

Figure 6.15 Representation of the 1-D cored model.

As expected, a lower stability of the cored cable is obtained at the 25% of the operating current *Fig. 6.17*, but surprisingly, at full current, the cored cable exhibits higher quench energies than the non-cored cable *Fig. 6.16*. Basically the core represent a link between the strands: at high currents it is a bridge, while at low currents it behaves like a wall. This strange results are due to the heat capacity of the core. Simulating the core as a single thermal element, each strand can use the whole heat capacity of the core for the heat exchange, and this represent an overestimate of the core role. Removing the heat capacity of the core, i.e. it is not considered as a thermal element anymore, and keeping the high values for the

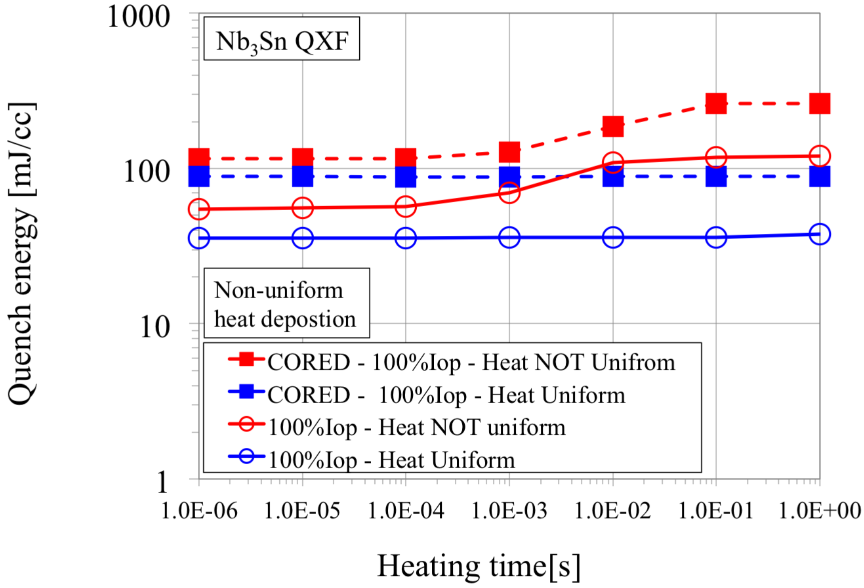

Figure 6.16 Comparison between cored and non-cored QXF Nb_3Sn cable at 100% of operating current : Quench energies vs. Heating time at the operating current, with non-uniform heat deposition.

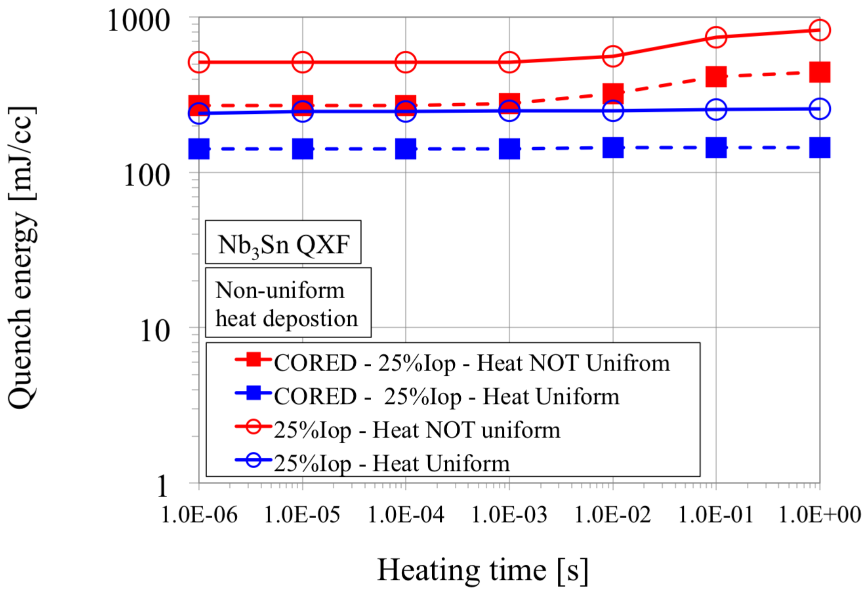

Figure 6.17 Comparison between cored and non-cored QXF Nb_3Sn cable at 25% of operating current : Quench energies vs. Heating time at the operating current, with non-uniform heat deposition.

thermal and electric resistance between non-adjacent strands, the same results of the non-cored cable can be observed in *Fig. 6.18*. In conclusion, for a complete and more accurate analysis, the core should be split in several thermal elements, each one linked with the neighbouring strands. However it is easy to understand that this model upgrade implies a strong increase of the model complexity and computational time.

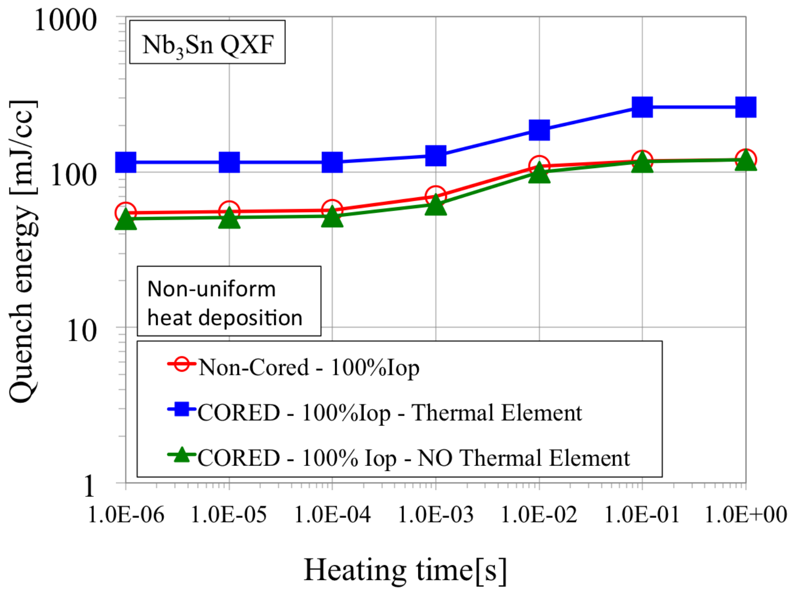

Figure 6.18 Comparison between non-cored and cored with and without the core heat capacity: Quench energies vs. Heating time at the operating current, with non-uniform heat deposition.

7. Conclusion

This work analyses the stability margin of the Nb_3Sn MQXF Rutherford cables for the High Luminosity Large Hadron Collider project of the European Organization for Nuclear Research - CERN. Different cable models at increasing levels of complexity and detail have been analysed: 0-D, 1-D with *1-strand* and *N-strand* models. The impact on quench energy of a resistive core embedded between the two layers of the Rutherford cables has been studied. The comparison between the quench energy values obtained for the Nb_3Sn conductor in the working conditions of the LHC Hi-Lumi inner triplet low-β quadrupole (MQXF) and those of the NbTi Rutherford cable of the LHC main quadrupole magnet (MQ) has been presented.

Regarding uniform magnetic field distribution and uniform heat deposition, the results for the 0-D and the 1-D models are in very good agreement. The Nb_3Sn cables exhibit a very strong local behaviour at fast time scales, highlighted by the limited current and heat exchange between neighbouring strands and the very small increase of the quench energy from the *1-strand* to the *N-strand* model. Furthermore, a strong dependance of the stability margin has been found on the spacial details of the heat deposition.

Several analyses have delineated the negligible contribution to the stability margin from the stabiliser and insulator. On the other hand, the absence of interstitial helium in MQXF cables determines a severe reduction of the quench energies, especially for transient heat disturbances.

Finally, despite the more demanding operating conditions for the magnets, the simulations for the MQXF Nb_3Sn cables give comparable quench energies with the actual LHC MQ $NbTi$ cables, at fast time scales.

8. Appendix A - Convergence studies

8.1 Integration time steps

In order to obtain solid results, it is necessary to know how the different choice of integration time steps influences our simulations. If the time of evolution of our simulation is observed with a too large step, there is the serious risk of losing critical information; for example temperature and/or current variations, that could be fundamental either for the quench or for the recovery, could be missed. On the other hand, using a too small time step implies a large increase in computational time and in memory. It is needed to find the right compromise between these two extremes: to obtain reliable results without using too many resources, in sense of computation time and memory space. Two cases of study has been chosen:

- one strand (one thermal, 0 electric component) :
  analysis of thermal time constants of the system

- three strands (3 thermal, 3 electric components) :
  analysis of thermal and electric time constants of the system

This kind of analysis for a higher number of strands became too time consuming, yet it also represents a repetition of the 3-strand case: the electro-thermal time constants are not expected to change relevantly. For each case, the dependence of the Minimum Quench Energy (MQE) with respect to the minimum and maximum integration time steps has been analysed. The other simulation parameters are taken as constant: the values are shown in *Table 8.1*.

It is important to underline that the simulations results are obtained following a convergence criterion of less than 5%. Stability variations below this value are not taken into account.

TimeMethod	EulerBackward
MeshType	uniform
NrElements	400
ElementOrder	1
ElementNodes	2
StepEstimate	smooth
ErrorEstimate	halving
ErrorControl	on
Tolerance	1.0E-07

Table 8.1 The constant parameters for the time step analysis

8.2 Thermal component

As mentioned above, it has been analysed both the thermal and the thermo-electric cases, with the aim of understanding the order of magnitude of the different time constants of the system. This allows the selection of proper integration time steps, in order to follow the evolution of the process with the correct time constant, which is a characteristic of the chosen physics. One thermal and zero electric element has been selected, with the purpose to analyse only the thermal characteristic of the system. The results, for the minimum and maximum integration time steps, are presented below.

8.2.1 Maximum integration time step

For this analysis the minimum time step value has been fixed equal to 1.0E-09 seconds and the maximum one increased, from 1.0E-9 seconds to a reasonable value, depending on the heat disturbance duration. The dependence of the MQE on the maximum integration time steps are presented in the *Fig. 8.1* and *Fig. 8.2*
The variation due to the increase of the maximum time step is in the same order of magnitude of the chosen convergence criterion ($< 5\%$). This is probably correlated with the very small value of the tolerance used for these simulations.

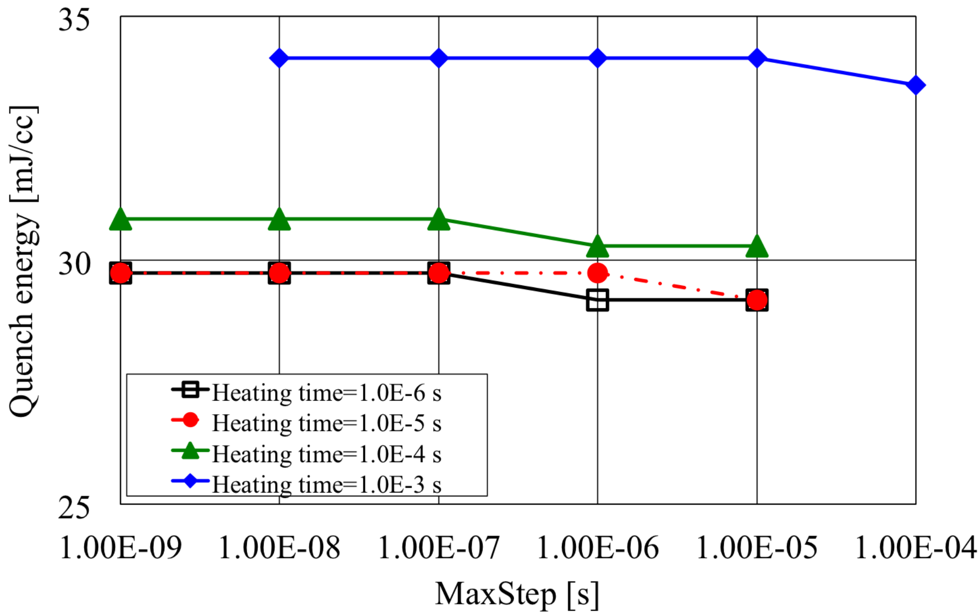

Figure 8.1 Stability of the Minimum Quench Energy in terms of maximum integration time steps. [Thermal component]

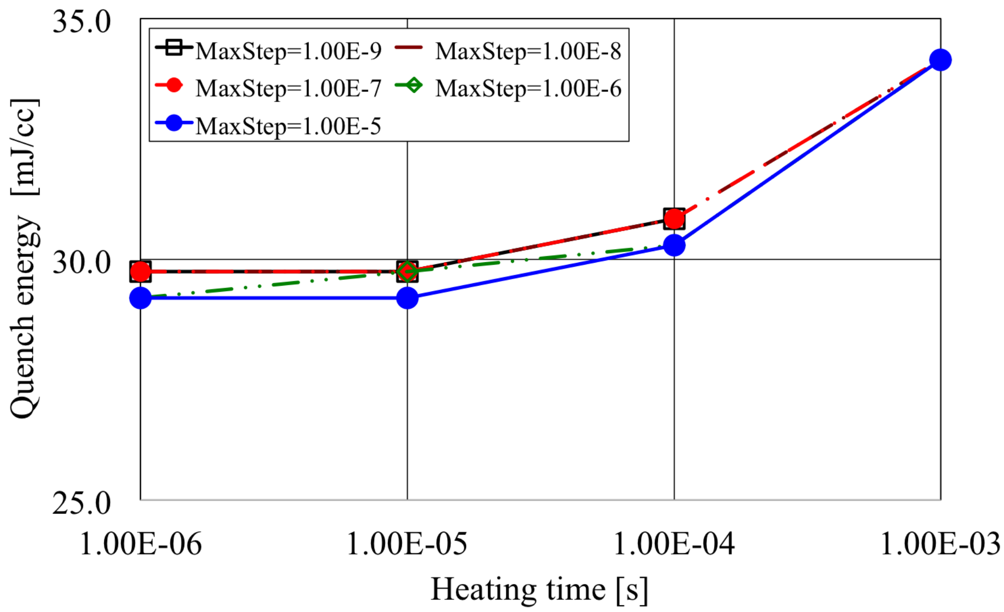

Figure 8.2 Minimum Quench Energy as a function of heat disturbance duration, with different maximum integration time steps. [Thermal component]

8.2.2 Minimum integration time step

In order to study the variations of the results due to the different minimum time steps, equal values for minimum and maximum steps have been set. These values are chosen from 1.0E-9 seconds to one tenth of the heat disturbance duration. The results are shown in *Fig. 8.3* and *Fig. 8.4*.
In this case, the variation of the MQE is more evident and not negligible. This is the demonstration that, if the evolution of the system is not followed using the correct time steps, important errors can occur.

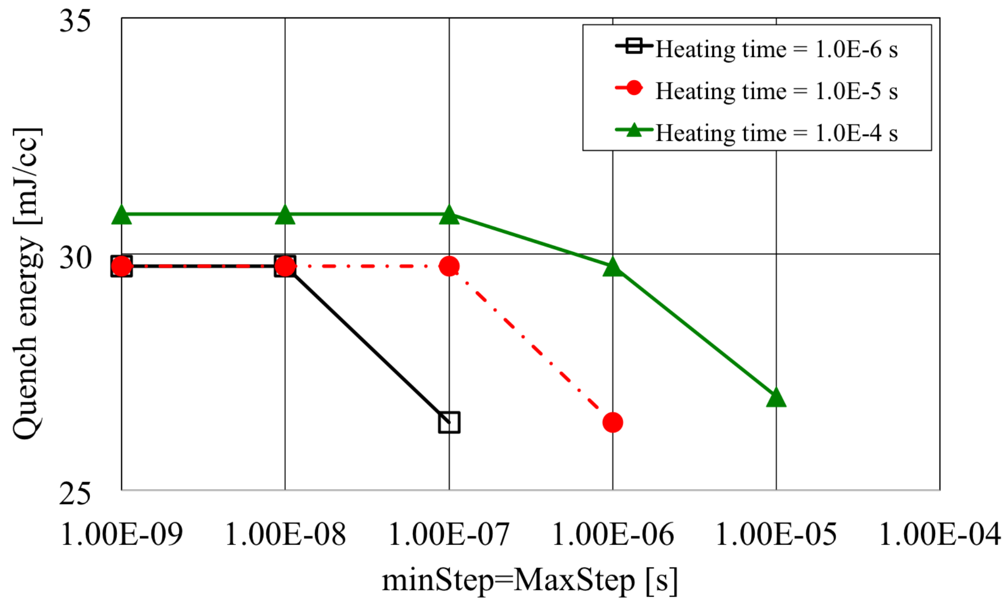

Figure 8.3 Stability of the Minimum Quench Energy in terms of minimum integration time steps. [Thermal component]

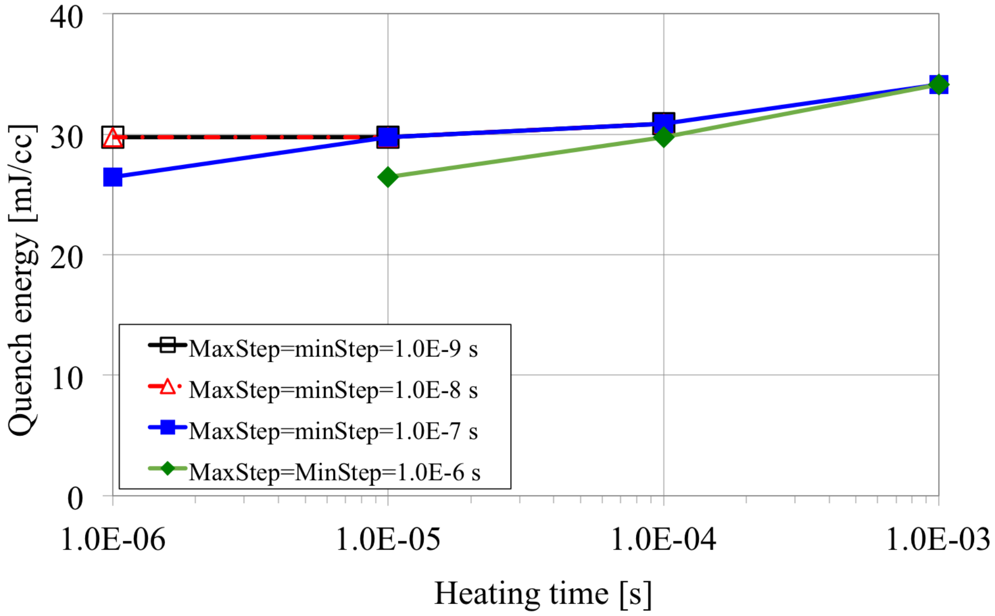

Figure 8.4 Minimum Quench Energy as a function of heat disturbance duration, with different minimum integration time steps. [Thermal component]

8.3 Thermal and Electric components

Taking into account the thermo-electric components the system can be analysed in a more accurate way. Three strands have been simulated, where both thermal and electric time constants, characteristic of the process, are considered. The procedure for the time integration analysis is the same as presented above for maximum and minimum steps. The results for this multi-strand investigation are shown in the *Fig. 8.5*, *Fig. 8.6*, *Fig. 8.7* and *Fig. 8.8*.

8.3.1 Maximum integration time step

As the *Fig. 8.5* and the *Fig. 8.6* exhibit, there is no significant variation with respect to the *"only thermal"* case. For thermo-electric simulations the variations, which occurred for a different integration maximum time step, are comparable to the maximum error due to the convergence criterion.

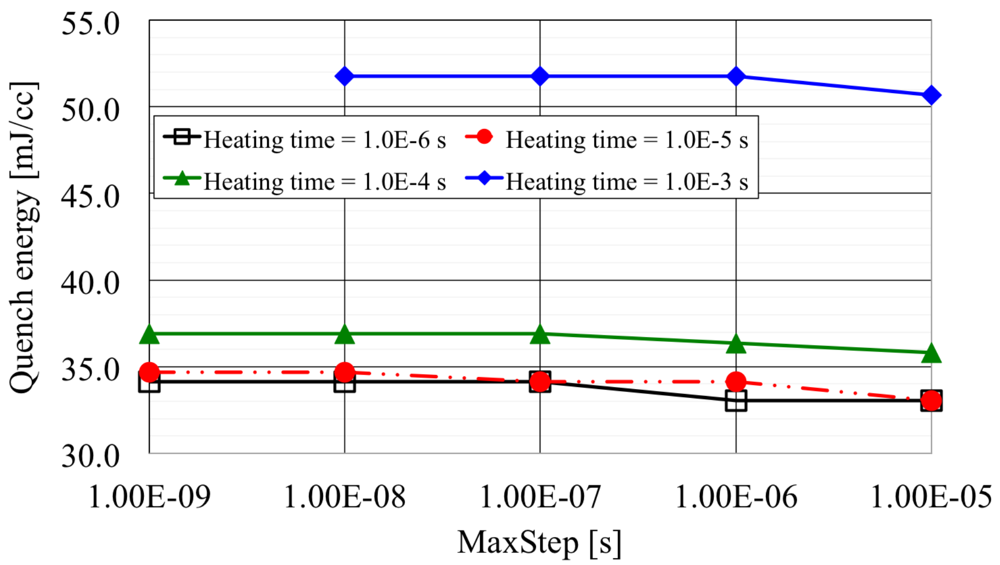

Figure 8.5 Stability of the Minimum Quench Energy in terms of maximum integration time steps. [Thermal and electric components]

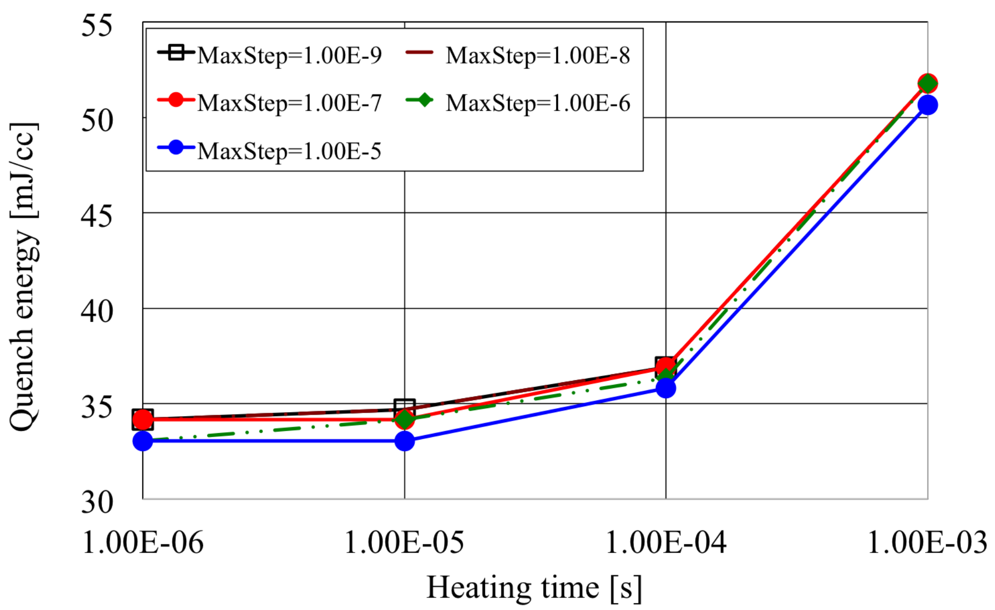

Figure 8.6 Minimum Quench Energy as a function of heat disturbance duration, with different maximum integration time steps. [Thermal and electric components]

8.3.2 Minimum integration time step

As expected, the results for the minimum steps are the same of the previous case: a flat behaviour of the Minimum Quench Energy can be observed until a certain value of minimum step, and then an unavoidable drop occurs. These similarities between the thermal and thermo-electric analyses imply that the characteristic time constants of the thermal exchange are smaller in comparison with electric ones. This means that the process is dominated by the thermal exchange, which is, as just said, faster than the electrical phenomena.

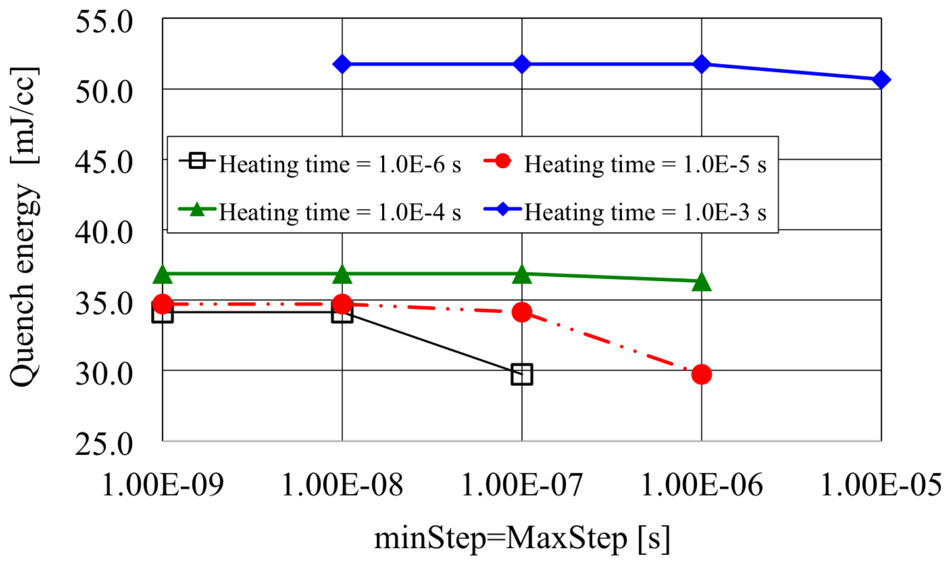

Figure 8.7 Stability of the Minimum Quench Energy in terms of minimum integration time steps. [Thermal and electric components]

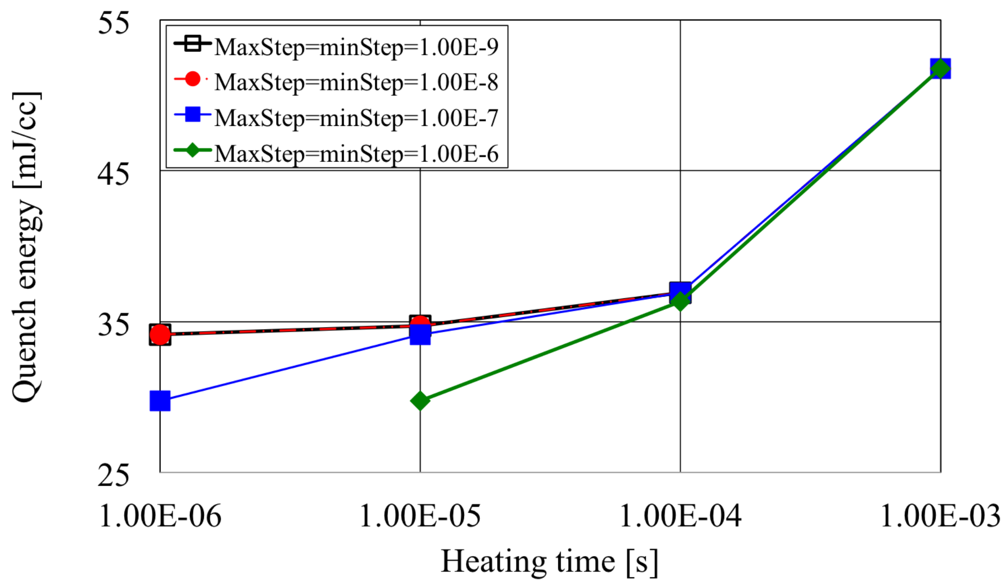

Figure 8.8 Minimum Quench Energy as a function of heat disturbance duration, with different minimum integration time steps. [Thermal and electric components]

According to the results presented above, the *"standard"* values for the maximum and minimum integration time steps can be defined. The suggested values, varying during the simulation time evolution, are shown in *Table 8.2*.

Simulation Time	Minimum time step	Maximum time step
from 0.0 sec to 1.0E-5 sec	1.0E-8 sec	1.0E-7 sec
from 1.0E-5 sec to 1.0E-3 sec	1.0E-7 sec	1.0E-6 sec
from 1.0E-3 sec to END	1.0E-6 sec	1.0E-5 sec

Table 8.2 Standard values for maximum and minimum integration time steps

The choice of bigger step values could represent a risk in terms of simulation's reliability. The maximum achievable step is limited to 1.0E-5 seconds, in order to avoid errors due to a coarse time evaluation of the system*. On the other hand, a selection of smaller steps or a not incremental choice, implies a huge consumption of computational time and memory.

*The maximum time step of 1.0E-5 seconds represent an advice, rather than a limit. If the simulations are too time consuming, this value can be modified, e.g. it can be chosen equal to 1.0E-3 seconds, with the consciousness that some informations could be lost.

8.4 Tolerance

The tolerance is the: *"relative error to be achieved at each time step during time integration, used to control the time step"* [5] . This means that the importance of integration time steps cannot be analysed without paying attention to the used tolerance. Therefore, using the standard values of the *Table 8.2*, a study on the influence of the tolerance parameter, both for thermal case and for thermo-electric one, has been carried out. The results are presented in the *Fig. 8.9* and *Fig. 8.10*.

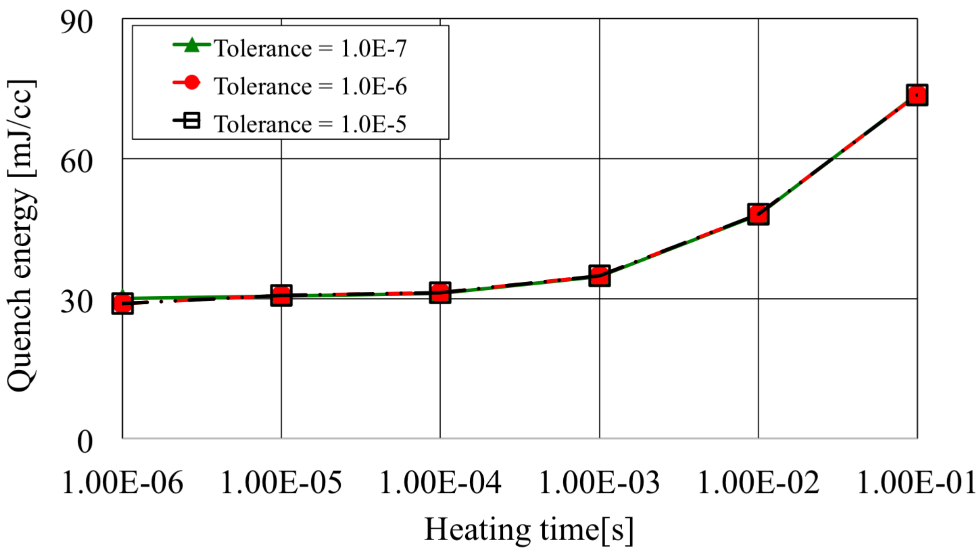

Figure 8.9 Stability of the Minimum Quench Energy in terms of tolerance. [Thermal component]

As *Fig. 8.9* and *Fig. 8.10*, except for very short disturbance, the curves are perfectly overlapped. This means that, with our choice of time steps, a results deviation due to the tolerance cannot be observed. However, the gradual increasing of the tolerance value is suggested, as it is shown in *Table 8.3*.

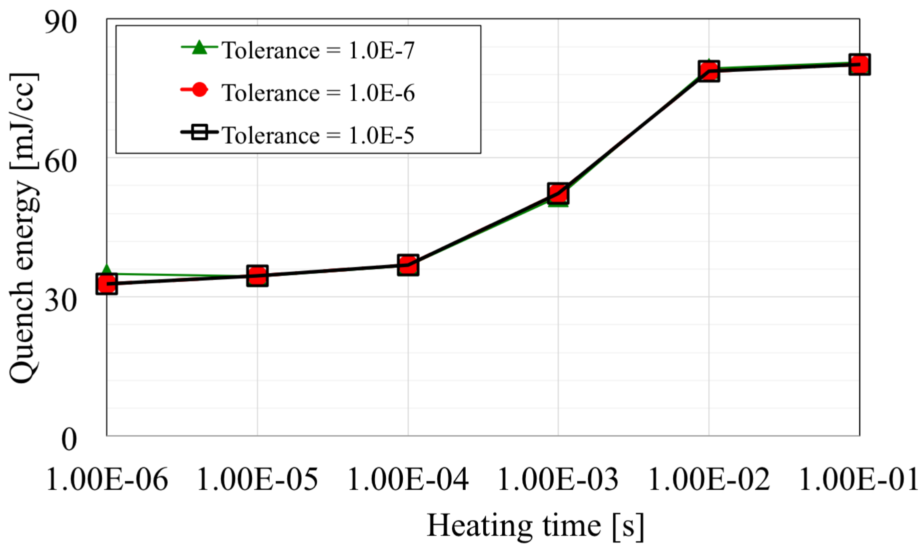

Figure 8.10 Stability of the Minimum Quench Energy in terms of tolerance. [Thermal and electric components]

Simulation Time	**Tolerance**
from 0.0 sec to 1.0E-5 sec	1.0E-7 sec
from 1.0E-5 sec to 1.0E-3 sec	1.0E-6 sec
from 1.0E-3 sec to END	1.0E-5 sec

Table 8.3 Standard values for tolerance

8.5 Mesh dimension

Once it has been understood how to deal with time parameters, it is necessary to analyse spacial dimension convergence. The number of mesh elements, or the size of a mesh element, represents a problem similar to the integration time steps one: if a too big mesh element is used, critical information can be lost. On the other hand, if a too dense mesh is chosen a huge quantity of simulation time is needed. With the aim of avoiding these inconveniences another convergence study has been performed, analysing the stability of the minimum quench energy in terms of the size of mesh elements. The size of a mesh element is given by this obvious correlation

$$D_x = \frac{L}{n} \tag{8.1}$$

where s is the size of the element, n is the number of elements and L is the length of the system (in our simulation $L = 2\ m$). The results of this analysis are shown, for thermal and thermo-electric components, in the *Fig. 8.11* and in the *Fig. 8.12*.

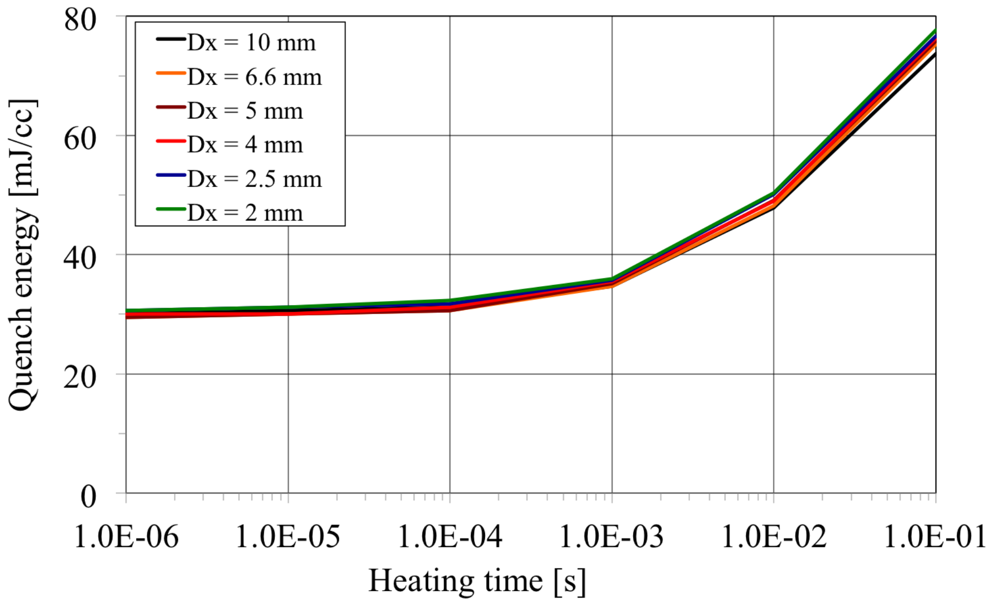

Figure 8.11 Stability of the Minimum Quench Energy in terms of mesh element number . [Thermal component]

An increase of the minimum quench energy with increasing number of elements can be observed, especially for higher value of disturbance time. However, these

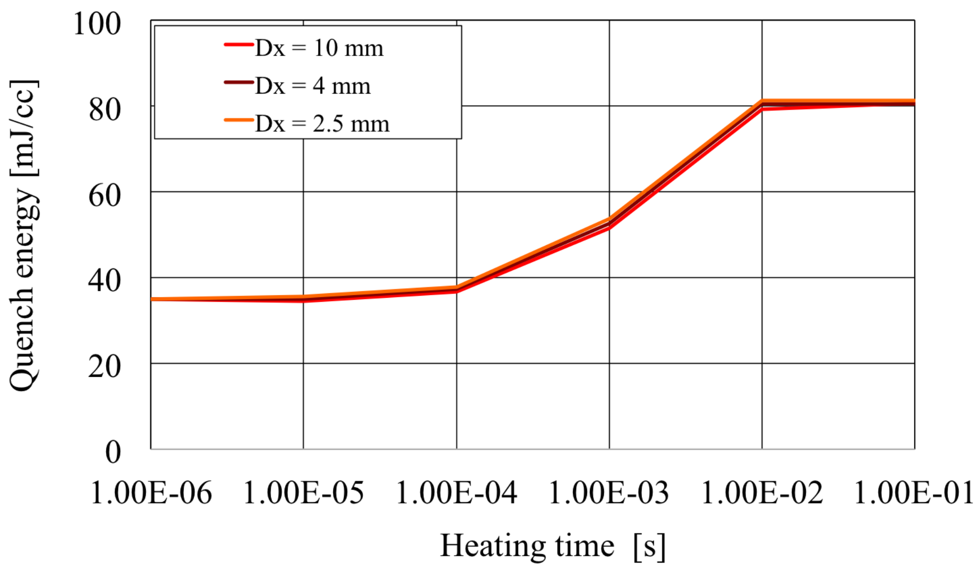

Figure 8.12 Stability of the Minimum Quench Energy in terms of mesh element number for long heat disturbance . [Thermal and Electric components]

variations are in the same order of magnitude as the simulation precision (*5%*) and therefore can be considered acceptable. In conclusion, a large number of mesh elements are not required, unless we need a high accuracy of results. Obviously, the more we increase the number of the mesh elements, the more the computational time becomes elevated.

8.6 Error control

Finally, another parameter that is strongly correlated with the computational time of our processes is to be taken into account. If the Error Controll is ON: *"at each time step a check is performed to verify that the integration error is below the specified Tolerance. If this is not the case the time step is changed and the integration is tried again, iterating until the tolerance error is reached [...] The iteration can significantly increase CPU time."* [5] As written in *Table 8.1*, the previous analyses are performed with the activated error control. Now, it is important to verify if the chain of this strong control system can be broken, and consequentially save a large amount of computational time. Also for this last analysis the thermal and the thermo-electric cases are taken into account, both with the parameters of the *Table 8.2*.

The *Fig. 8.13* and the *Fig. 8.14* are the demonstration that, under the aforementioned operating condition, there is no need to check the integration error at each time step; therefore a remarkable amount of computational can be saved time without losing any important information.

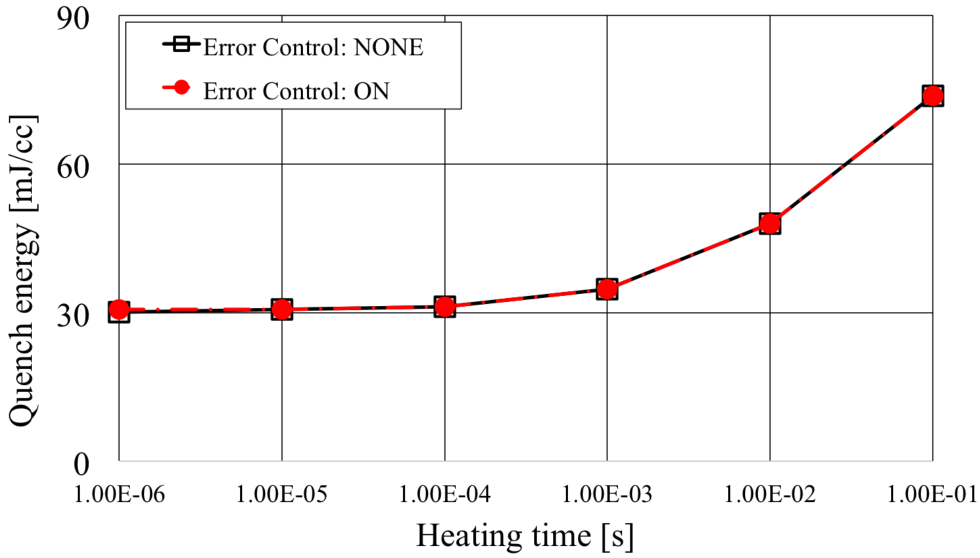

Figure 8.13 Stability of the Minimum Quench Energy in terms of error control. [Thermal component]

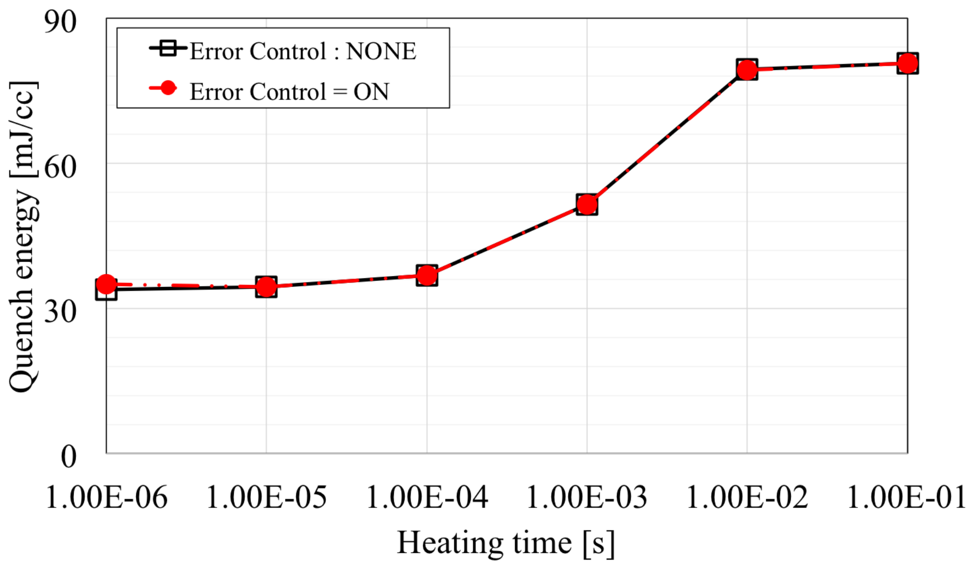

Figure 8.14 Stability of the Minimum Quench Energy in terms of error control. [Thermal and electric components]

9. Appendix B - Hitchhiker's guide to the Linux and LxPlus galaxy

If you are reading this *"guide"* you are probably working with (or for, depending on the points of view) Luca Bottura and Marco Breschi. I'm writing these few lines just to explain what I have done and what you could (NOT should) do in order to avoid some annoying problems concerning disconnections from LxPlus cluster, disappeared NOHUP processes from somewhere and similar stuff, that probably will drive you crazy in a couple of days. First of all an LxPlus account is not thought for long and intense simulation: *"The service is intended for interactive work [...] Jobs consuming lots of CPU for extended periods of time will be killed automatically"*.You will notice (or, if you are reading this secret guide, you have already noticed it) that if you try to run a simulation for a whole night, when you are in your warm bed, sleeping deeply, or in the pub, drinking your cold beer, this simulation will unavoidably CRASH!

DON'T PANIC: the solution is just right here! You should use the nohup command.

```
  nohup ./program.exe &
```

Caution! You will never see anymore the outputs on your screen, but all those lines are saved in a file called *something.out*. After few hours of simulation this file can easily reach a huge dimension and it could create several problems, due to the annoying memory limit of LxPlus account. You can ask politely to the Desk Service to enlarge your memory space to reach the maximum limit of 10Gb (*"if you need more, you can create personal workspace on AFS"*), but, in any case, I strongly recommend you to not to create this .out file. It's just a nice, huge and useless text file on your folder and you can avoid it using the command below:

```
nohup ./program.exe 2\%>1 null &
```

At this point you could reply: *"Thank you genius! How can I control my processes now?!?"*.

DON'T PANIC: I'm here for you, mate!

With the top command you can have a look to the running processes list and you can get the PID (identification number) of THEA. You can rename the *thea.bin* file in a different way, for example THEA01 or THEA42, in order to be sure that you are watching to the right THEA process. Important: you MUST remember to change the type of permission on the modified .bin files:

```
chmod +x THEA42.bin
```

Once you have the PID you have to power to make a choice:

- strace : trace system calls and signals

  ```
  strace -p (PID) -s (strg)
  ```

- kill : terminate a process

  ```
  kill -9 (PID)
  ```

Important: if you want to use these commands or run a THEAPOST process while the simulation is still running you must be connected to the same *"node"* of the network. What I mean is that when you log-in with your LxPlus account, you are accessing to a specific machine with a specific IP address, e.g. 188.184.xx.xx. Connecting your self at this address is easy:

```
ssh accountname@188.184.xx.xx
```

When you are connected you can verify the IP address using:

```
ifconfig
```

and check the *“inet addr”* line.

Okay, here we are. Now you have a simulation running on a machine of the cluster and you can be sure that, until your section is open and your connection works properly, it doesn't crash. New problem: what happens if a disconnection suddenly occurs or if your stupid colleague decides to play with the power outlet of your computer? **DON'T PANIC!**: we have a solution for this too. According to the LxPlus Service Desk, you have to follow this procedure: https://cern.service-now.com/service-portal/article.do?n=KB0002408

```
krenew
AKLOG=/usr/bin/aklog krenew -b -t -- screen -D -m
screen -r
```

Now you have the power to use the LxPlus *“force”* for more or less 1 weak per simulation (I haven't yet understood why my simulation crashes after 6 or 7 days of running), also disconnecting your device from the cluster. What I suggest to do, is to create little tiny Fortran program, that allows you to call whenever and how many time you want a THEA process.

```
call SYSTEM("./runthea cable.input")
call SYSTEM("./runtheapost cable.post")
```

where *runthea* and *runtheapost* are two executable files containing respectively:

```
echo $1 > tmp
~/CryoSoft/bin/thea < tmp
rm tmp
```

```
echo $1 > tmp
~/CryoSoft/bin/theapost < tmp
rm tmp
```

These two microscopic and fundamental files are just two text files, converted in .exe through:

```
chmod +x runthea
```

It's all for now, my friend. I spent too much time and energy to discover the stupid things listed above, and I hope that you can save time and mental health using this brief guide. If you want, you can (YOU MUST) update this list with your knowledge and your wisdom, in order to save someone else's life.

Good luck my friend, and do not forget your towel: it is about the most massively useful thing an interstellar hitchhiker can have!

For every doubt, explanation and complaint do not hesitate to contact me at:

enrico.felcini@gmail.com

Bibliography

[1] E. Cavanna and et al, *Design of the Nb3Sn Inner Triplet.* FP7 High Luminosity Large Hadron Collider Design Study, 04 September 2015.

[2] G. Battistoni and F. Cerruti, *The FLUKA code: description and benchmarking.* Proc. Hadronic Shower Simul. Workshop, FermiLab,AIP, 2007.

[3] L. Bottura, *JC Parameterization for ITER Nb3Sn Production.* 2008.

[4] L. Bottura, *CryoSoft Code ZeroDee v. 1.3.* January 2001.

[5] L. Bottura, *CryoSoft code THEA v. 2.2.* December 2013.

[6] L. Bottura, C. Rosso, and M. Breschi, *A general model for thermal, hydraulic and electric analysis of superconducting cable.* Workshop on Computation of tHermo-hydrAulic Transient in Superconductors, Frascati, Italy, September 6, 2000.

[7] G. Willering, *Stability of superconducting Rutherford cables for accelerator magnets.* PhD Dissertation, University of Twente, The Netherlands, 2009.

[8] P. P. Granieri, *Heat Trasnfer between the Superconducting Cables of the LHC Accelerator Magnets and the Superfluid Helium Bath.* PhD Dissertation, Ecole Polythechnique Fèdèrale de Lausanne, Suisse, 2012.

[9] M. Breschi, A. Bevilacqua, L. Bottura, and P. P. Granieri, *Analysis of beam-induced quenches of the LHC cables with a multi-strand model.* , IEEE Transaction on applied Superconductivity , vol. 25, 4700405, August 10, 2014.

[10] L. Bottura, "Cable stability," *CERN Yellow Report CERN-2014-005, pp.401-451.*

[11] *http://home.cern.*

[12] W. Herr and B. Muratori, *Concept of luminosity.* CERN Accelerator School: Intermediate Course on Accelerator Physics, Zeuthen, Germany, 15-26 Sep 2003.

[13] H. K. Onnes, *Notes.* Phys. Lab. Univ. Leiden, 1911.

[14] W. Meissner and R. Ochsenfeld, *Ein neuer Effekt bei Eintritt der Supraleitfähigkeit.* Naturwissenschaften, 1933.

[15] H. L. F. London, "The electromagnetic equations of the supraconductor," *Proceedings of the Royal Society A: Mathematical, Physical and Engineering Sciences*, 1935.

[16] J. Bardeen, L. N. Cooper, and J. R. Schrieffer, *Theory of Superconductivity.* 1957.

[17] J. G. Bednorz and K. A. Müller, *Possible high Tc superconductivity in the BaLaCuO system.* Zeitschrift für Physik B Condensed Matter, June 1986.

[18] M. K. Wu and et al., *Superconductivity at 93 K in a New Mixed Phase YBaCuO Compound System at Ambient Pressure.* 1987.

[19] S. Bud'ko, G. Lapertot, C. Petrovic, C. E. Cunningham, N. Anderson, and P. Canfield, "Boron isotope effect in superconducting mgb2," 26 February 2001.

[20] A. Priebe, "Quench tests of lhc magnets with beam: studies on beam loss development and determination of quench levels," *Ph. D. Dissertation, Ecole Polytechnique Federale de Lausanne, Lausanne, Switzerland*, 2014.

[21] J. B. Jeanneret, L. O. D. Leroy, and T. Trenkler, "Quench levels and transient beam losses in lhc magnets," *LHC Project Report 44*, 1996.

[22] B. Auchmann and et al., "Testing beam-induced quench levels of lhc superconducting magnets," *Phys. Rev. ST Accel. Beams 18, 061002*, 2015.

[23] L. Rossi and L. Bottura, "Superconducting magnets for particle accelerators," *Reviews of Accelerator Science and Technology Vol. 5 (2012) 51–89. World Scientific Publishing Company.*

[24] S. Bermudez, *MQXF 2nd generation design.* Joint HiLumi LHC-LARP Annual Meeting/24th LARP Collaboration Meeting, 12th May, 2015.

[25] H. Katheder, *Optimum thermohydraulic operation regime for cable in conduit superconducotrs (CICS).* Cryogenics 34, pp.595-598, 1994.

[26] F. Grover, *Inductance Calculations.* Ed. by Dover Publicatio, New York: Mineola, 2004.

[27] M. Calvi, M. Breschi, and P. Ribani, *Analysis of the inductance coefficients in multistrand cables: analytical, numerical and experimental resutls.* IEEE Transaction on applied superconductivity 15, 2005.

[28] S. Bermudez, *Private Communication.* CERN, 2015.

[29] M. Massimini, *Electrical and thermal analysis of superconducting wires and LHC cables.* Master degree dissertation, University of Bologna, Italy, 2013.

[30] A. Bevilacqua, *Stability Analysis of the LHC superconducting cables with a Multi-Strand model.* Internal CERN Report, 26th February 2015.